

Review: Coefficients for Stress, Temperature, and Composition Effects in Fluorescence Measurements of Alumina

Robert F. Cook and Chris A. Michaels

National Institute of Standards and Technology,
Gaithersburg, MD 20899, USA

robert.cook@nist.gov
chris.michaels@nist.gov

The numerical coefficients linearly relating the effects of stress (including pressure), temperature, and composition to shifts in the energies of the Cr-related fluorescence in alumina (Al_2O_3) are reviewed. The primary focus is the shift of the R_1 and R_2 “ruby” fluorescence lines under conditions typical for stress determination in polycrystalline Al_2O_3 . No significant experimental difference in the R_1 and R_2 responses is observed for hydrostatic stress (or pressure) conditions (average shift coefficient of about $7.6 \text{ cm}^{-1}/\text{GPa}$), changes in temperature (about $0.140 \text{ cm}^{-1}/\text{K}$), or variations in composition (about $120 \text{ cm}^{-1}/\text{mass fraction of Cr}$). There are significant differences in the R_1 and R_2 responses for nonhydrostatic stress conditions. In particular, for uniaxial stress along the a and c directions in the Al_2O_3 crystal, the R_1 piezospectroscopic tensor coefficients (about $3.0 \text{ cm}^{-1}/\text{GPa}$ and $1.6 \text{ GPa cm}^{-1}/\text{GPa}$, respectively) differ considerably, whereas the R_2 coefficients (about $2.6 \text{ cm}^{-1}/\text{GPa}$ and $2.3 \text{ GPa cm}^{-1}/\text{GPa}$, respectively) do not. Measurements of the piezospectroscopic tensor coefficients are shown to have interlaboratory relative consistency of about 4 % extending over 30 years, and are consistent with the scalar high-pressure measurements. Measurements of the temperature coefficients are shown to have interlaboratory relative consistency less than 1 % extending over 60 years. Fluorescence-based measurements of stress in polycrystalline Al_2O_3 , although requiring temperature adjustment, are shown to have a relative uncertainty of about 2.5 %.

Key words: alumina; chromium; crystal; fluorescence; polycrystal; ruby; sapphire; stress; temperature.

Accepted: November 28, 2017

Published: December 13, 2017

<https://doi.org/10.6028/jres.122.043>

1. Introduction

It has long been known that optical states in many compounds arise from the incorporation of “impurities” into the host compound—particularly visible examples are the colors of some oxide minerals [1]. The energies and transition probabilities of the optical states depend on the local atomic environment set by the host surrounding the impurity. In minerals, the states are usually well described by crystal field theory [1], which models the electronic band structure, and hence the optical absorption and emission spectra, of a positively charged impurity ion surrounded by negatively charged host ions arranged in a polygon (e.g., cube, tetrahedron, octahedron) set by the crystal lattice. The host negative ions are usually O^{2-} ions, and the positive impurity ions are usually first transition series outer electron d-shell ions (e.g., Fe^{2+} and Fe^{3+} in garnet and Cr^{3+} in emerald and ruby). The crystal field refers to the electric field the host ions set up at the impurity ion site, thereby perturbing the electronic structure of the impurity ion. Crystal field effects thus depend sensitively on the size, shape, and symmetry of the negatively charged oxygen ion array surrounding the positively charged impurity ion. Hence, factors that change the size, shape, or symmetry of the negatively charged array, e.g., mechanical stress, will change the crystal field and thus the optical absorption and emission characteristics of a mineral.

In particular, the limited (< 1 % by mol) substitution of Cr^{3+} for Al^{3+} in the Al_2O_3 corundum, α -alumina, structure leads to the formation of ruby. In its pure form, corundum (often known as “sapphire”)

consists of parallel sheets of triangularly coordinated O^{2-} ions with Al^{3+} ions in pairs occupying 2/3 of the octahedral interstices between the sheets [1, 2]. The sheets are perpendicular to the c axis ([0001] direction) of the structure and parallel to three equivalent a axes, a_1, a_2, a_3 ($\{2\bar{1}\bar{1}0\}$), which are in turn are separated by 120° and perpendicular to the c axis. The structure is trigonal, but often (well-) approximated as hexagonal. It is convenient to introduce a nonequivalent m axis parallel to the sheets ($\{01\bar{1}0\}$) and perpendicular to a_1 , such that $a-m-c$ form a right-handed, perpendicular coordinate system. A schematic diagram is shown in Fig. 1(a). The interstices are trigonally distorted octahedra formed by two triangles of O^{2-} ions in adjacent sheets; the triangles are rotated by 176° from each other, reducing the symmetry of the octahedra from C_{3v} to C_3 (the symmetry of the lattice is D_{3d}). In corundum, the Al^{3+} ions sit off-center in the octahedra, lying somewhat closer to the “upper,” smaller triangle of O^{2-} ions. Schematic diagrams are shown in Fig. 1(b) and Fig. 1(c). In ruby, Cr^{3+} ions substitute for some Al^{3+} ions, occupying similar octahedrally coordinated, off-center lattice positions. The Cr^{3+} ions are a little bit larger than Al^{3+} ions, with ionic radii of 64 nm and 57 nm, respectively, leading to elongation of the substituted octahedron along the c axis [3].

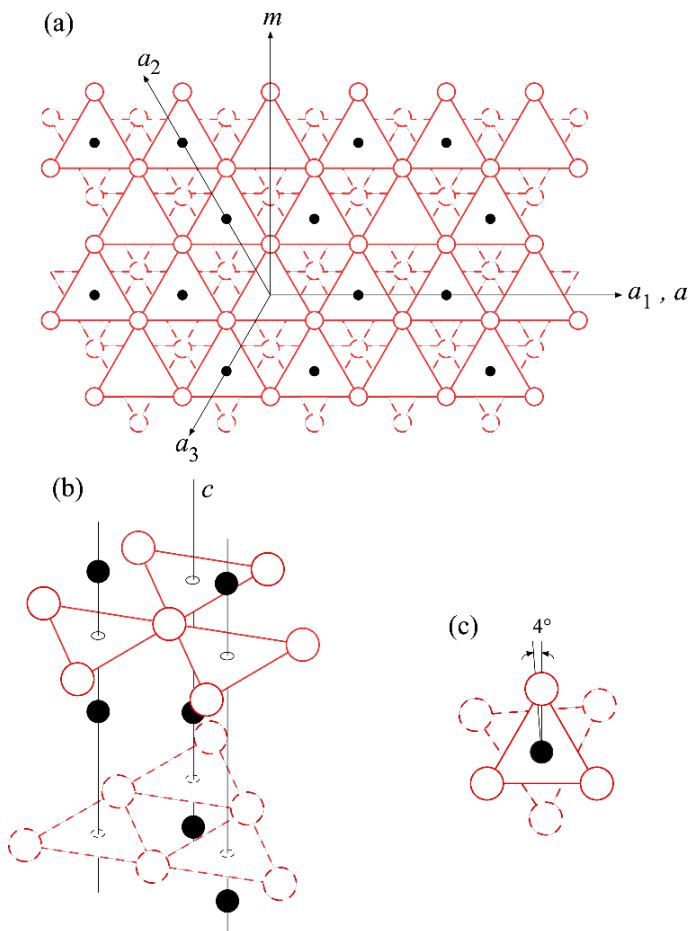


Fig. 1. (a) Schematic plan view of the α - Al_2O_3 structure, looking along the c axis and perpendicular to the three equivalent a_1, a_2 , and a_3 axes. The structure consists of triangularly coordinated O^{2-} ions (large circles) in sheets that alternate in antiparallel orientation along the c axis (the triangular coordination of two adjacent sheets is indicated by the solid and dashed lines). The Al^{3+} ions (small disks) occupy 2/3 of the interstices between the sheets and are octahedrally coordinated by the O^{2-} ions. (b) Schematic projection of the α - Al_2O_3 structure, looking perpendicular to the c axis. (c) Schematic plan view of the trigonally modified octahedral coordination of Al^{3+} by O^{2-} in α - Al_2O_3 showing one O^{2-} triangle (lower, dashed) slightly larger and rotated relative to the other (upper, solid). Figure is after Ref. [1]. The structures in (b) and (c) are idealized as equilateral triangles (see elsewhere for idealized a - and m -plane elevations).

The charged O²⁻ ions form an electric field, a “crystal field,” at the Cr³⁺ sites, with near-perfect (trigonally modified) octahedral symmetry, removing the degeneracy of the five *d* orbitals of free-ion Cr³⁺. An octahedral field leads to a low-energy configuration for Cr³⁺, consisting of electron occupation of three, low-energy *t*_{2g} orbitals and two empty, high-energy *e*_g orbitals. Electron-electron interactions lead to merging of the three *t*_{2g} orbitals into a singlet ground state labelled (spectroscopically) as ⁴A_{2g} [1]. Two important excited states for electrons in ruby are the ⁴T_{1g} and ⁴T_{2g} states, leading to broad optical absorption in the blue (the “Y” band, electron excitation from ⁴A_{2g} to ⁴T_{1g}, about 25 000 cm⁻¹ in energy) and in the yellow-green (the “U” band, electron excitation from ⁴A_{2g} to ⁴T_{2g}, about 18 000 cm⁻¹) regions of the spectrum, but leaving a visible “window” in the red (about 16 000 cm⁻¹ and less) region of the spectrum, giving ruby its distinctive red color [2]. The octahedral crystal-field states ⁴A_{2g}, ⁴T_{1g}, and ⁴T_{2g} are group-theoretical spin-allowed states deriving from the free-ion ⁴F ground state. The state of great importance here is the ²E spin-disallowed doublet state derived from the free-ion ²G excited state. Spin-orbit coupling splits the ²E doublet into two states, leading to two emission lines, R₁ and R₂, the “ruby” lines, coincidentally red, at energies of approximately 14 403 cm⁻¹ and 14 443 cm⁻¹ (about 1.79 eV, with wavelengths of about 694 nm [1, 2]). The process of interest here in ruby is Y and U optical absorption of photons, leading to excitation of electrons from the ⁴A_{2g} ground state to the ⁴T_{1g}, and ⁴T_{2g} states, followed by internal conversion of the energy of the electrons *via* the thermal phonon bath to the split ²E states, and, finally, R₁ and R₂ radiative fluorescence as the electrons descend from the ²E states back to the ⁴A_{2g} ground state (fluorescence lifetime of the ²E states is a few milliseconds [4]). A schematic diagram of the relevant ruby electronic structure is shown in Fig. 2.

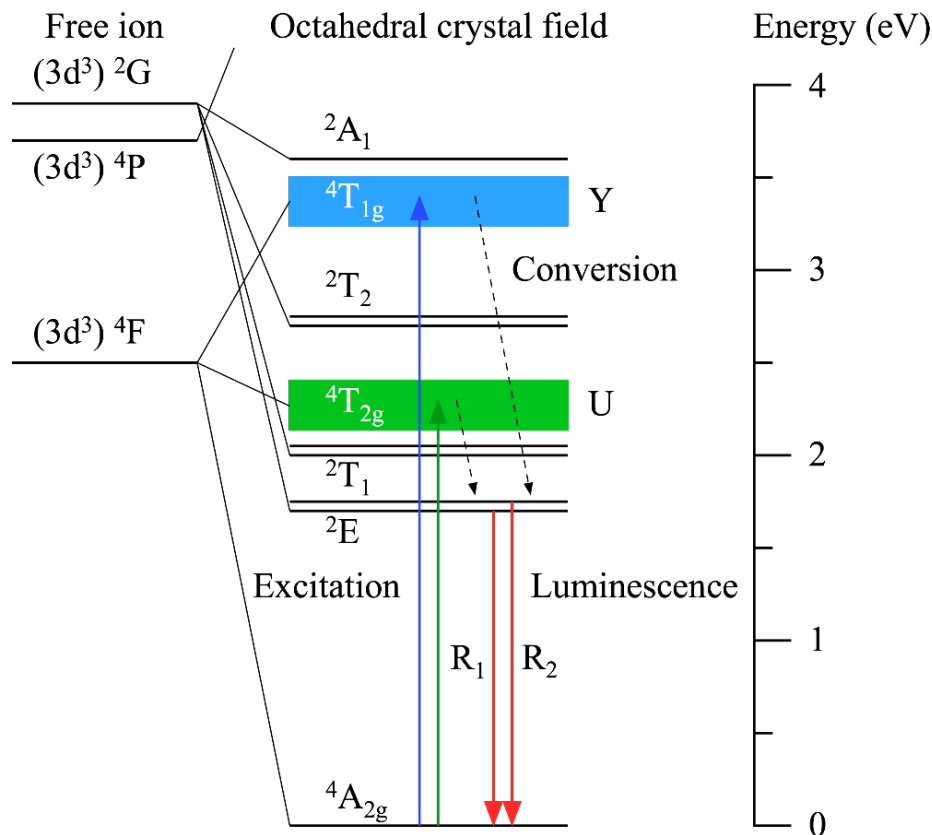


Fig. 2. Schematic diagram of the electronic energy levels of Cr³⁺ substituting for Al³⁺ in α -Al₂O₃ (ruby). The levels in the trigonally distorted octahedral ruby crystal field are shown in the center; the levels of the excited states of the free Cr³⁺ ion from which the crystal field levels derive are shown on the left. During ruby fluorescence, electrons are excited from the ⁴A_{2g} ground state to two strongly absorbing bands, in the green and blue regions of the spectrum, ⁴T_{2g} and ⁴T_{1g} (these absorptions are responsible for “ruby red”). The excited electrons interact with phonons in the structure, descending in energy to the split ²E states. The electrons then return to the ground state, emitting R₁ and R₂ fluorescent photons in the process. Figure is after Ref. [2].

Many spectroscopic studies have been performed on ruby and sapphire, investigating the states mentioned above and many others. A strong initial motivation, in the 1950s and 1960s, was testing of the then-nascent crystal field theory using the reasonably well-controlled Cr in Al_2O_3 ruby as the test vehicle [5–13]. An additional practical motivation at that time was detailed knowledge of the electro-optical energies of ruby, so that it could be used as a solid-state maser [14] and laser [15] material. It was clear to the early investigators that any factors straining the O^{2-} ion arrangement surrounding the Cr^{3+} ion led to changes in the crystal field and thus changes in the optical absorption and emission. Important factors were externally applied stress mediated by elasticity, temperature *via* thermal expansion, and composition *via* ionic radius mismatch. In the early 1970s, the process was turned around somewhat, and the details of crystal field theory were overtaken by empirical advances. In particular, calibrated experimental determination of shifts in the R_1 and R_2 line energies, ν , as a function of hydrostatic pressure [16–22] became the standard method for measuring pressure in high-pressure experiments involving the diamond anvil cell (DAC)—a method that continues to this day [23–37], although not without debate regarding calibration coefficients. (Here and throughout, citations within a topic are given in chronological order of publication.) An example of the fluorescence spectra for ruby and sapphire, demonstrating the composition effect, is shown in Fig. 3.

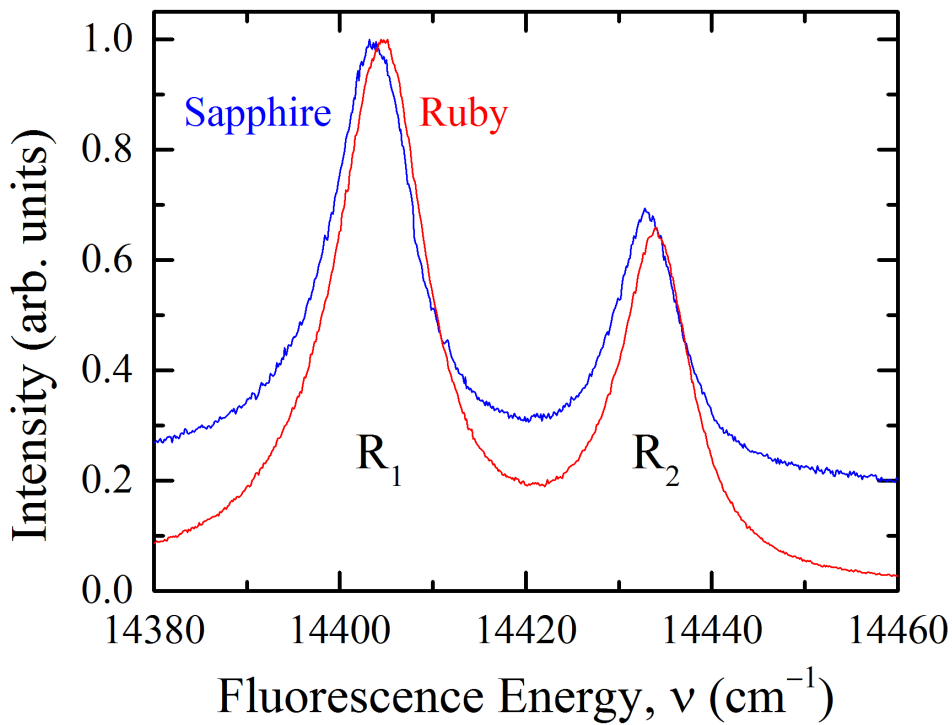


Fig. 3. Fluorescence spectra of single crystal sapphire and ruby, with the R_1 and R_2 peaks labelled. Sapphire ($\alpha\text{-Al}_2\text{O}_3$) usually contains enough Cr^{3+} to observe the peaks as here. The ruby peaks are shifted relative to the sapphire peaks due to Cr^{3+} composition effects. The ionic radius of Cr^{3+} is greater than that of Al^{3+} , such that on substitution of Cr^{3+} for Al^{3+} , an internal stress field is developed in the crystal, which shifts the fluorescence peaks due to a change in the crystal field. The ruby here contained 0.43 % mass fraction of Cr in $\text{Al}_2\text{O}_3\text{:Cr}$. Spectral intensities were adjusted for ease of comparison.

In the late 1970s, a mechanical model was developed by Grabner for nonhydrostatic loading (i.e., described by a general stress tensor) and applied to polycrystalline alumina [38]. At least part of the motivation for the polycrystalline research was to investigate the stress fields arising in polycrystalline alumina responsible for microcracking—the spontaneous localized cracking that occurs in polycrystalline alumina on cooling as a consequence of the anisotropic structure and thermal expansion of corundum [39–41]. From the 1990s onward, although there were many notable fundamental studies of the phenomenon [42–58], the shift in energy of R lines with stress was largely confined to the applied domain, detailed in numerous works, such as: measurement of stress in bulk Al_2O_3 polycrystals [42, 58–67]; in bulk Al_2O_3 - ZrO_2 composites [68–78]; in sapphire or composite fibers, free or in matrices [79–91]; in single-crystal thin films [92–95]; (particularly) in polycrystalline thick films on thermal barrier coatings [96–119]; and adjacent to introduced indentations, cracks, and scratches in Al_2O_3 and its composites [42, 120–134]. The works of Clarke and colleagues are notable for their advances in both the fundamental and applied domains (especially polycrystalline films) and also the works in the applied domain of Young and colleagues (fibers), Pezzotti and colleagues (cracks), and Todd and colleagues (indentations). An example of the shifts in the R_1 and R_2 fluorescence peaks arising from stress state changes is shown in Fig. 4.

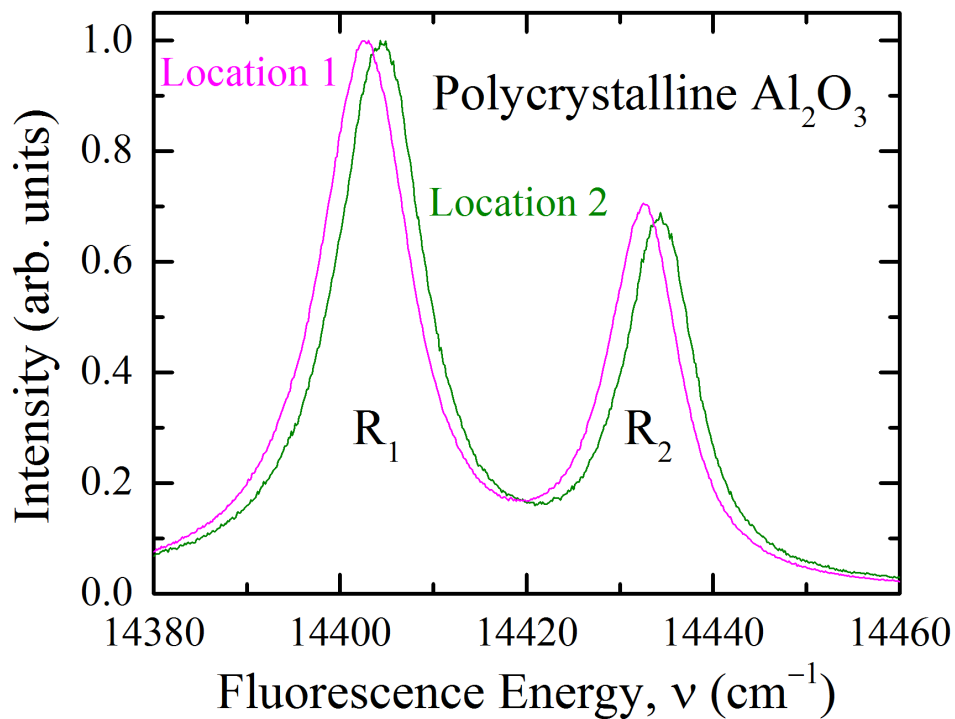


Fig. 4. Fluorescence spectra showing the R_1 and R_2 peaks obtained from two different locations in a Cr-doped polycrystalline Al_2O_3 material. The spectra are shifted relative to one another due to microstructural effects, leading to an internal stress field arising in the polycrystalline material from the thermal expansion anisotropy effects of the constituent Al_2O_3 grains. The spectra have been corrected for thermal effects and adjusted in intensity for easy comparison. Figure is after Ref. [67].

A feature of all the above work is that the shift in the R lines with external factors was taken as *linear*. That is, the shifts in the R-line energies were taken as simply proportional to the stress, temperature, or composition, in the first case as a tensor relation and in the last two as scalar relations. It is true that measured over large pressure or temperature ranges (more than 100 GPa or 100 K, where commonly used units for pressure are 1 Mbar = 100 GPa, 1 kg/cm² = 9.8×10^4 Pa, and 1 dyn/cm² = 0.1 Pa), the variation of R-line energies is extremely nonlinear (see equations in Ref. [2] used to generate Fig. 5). However, in the range of typical fluorescence measurements on typical polycrystalline alumina structures (variations less than 1 GPa, a few Kelvin), the dependence of the energies on stress, temperature, and composition *can* be taken as linear; see Fig. 5 [135].

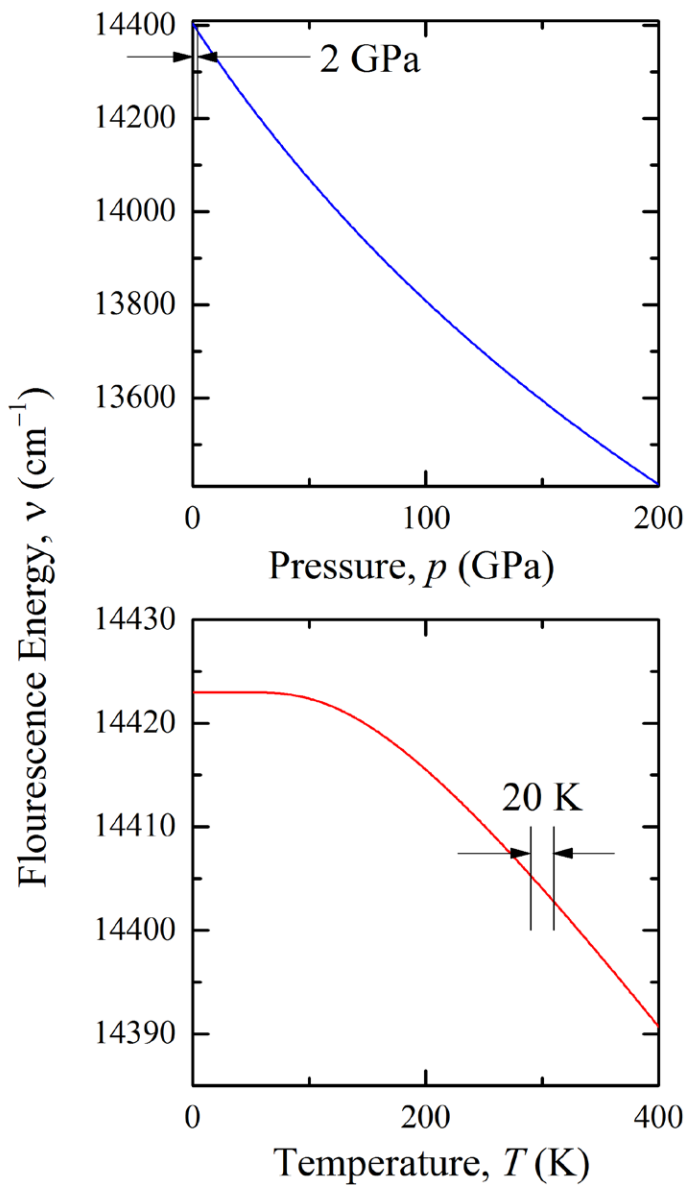


Fig. 5. Variations of R₁ fluorescence energy with (a) hydrostatic pressure and (b) temperature. The slight nonlinearity with pressure is only observed in high-pressure apparatus that access extremely high pressures. The small stress range (about 2 GPa) observed in typical Al₂O₃ microstructures is indicated and well described by a linear response. The nonlinearity with temperature is only observed in cryogenic apparatus that access extremely low temperatures. The small temperature range (about 20 K) occurring in typical measurements of Al₂O₃ microstructures is indicated and well described by a linear response.

Within the small variation approximation, the effects of stress, temperature, and composition are also taken as separable and additive:

$$\Delta\nu = \Delta\nu_\sigma + \Delta\nu_T + \Delta\nu_C, \quad (1)$$

where $\Delta\nu$ is the total shift in the (center) energy of an R-line emission peak, and $\Delta\nu_\sigma$, $\Delta\nu_T$, and $\Delta\nu_C$ are the individual contributions to the total shift from stress (σ), temperature (T), and composition (C) effects, respectively [135]. An example detailing the notation is shown in Fig. 6, where the center frequency in an unaffected system is ν_0 (say, in single-crystal sapphire), such that the total shift is given by $\Delta\nu = \nu - \nu_0$ (say, in polycrystalline alumina). Usually, it is stress measurement that is of the most interest, and hence Eq. (1) is often thought of as

$$\Delta\nu_\sigma = \Delta\nu - \Delta\nu_T - \Delta\nu_C, \quad (1a)$$

where temperature and composition effects “correct” the measured total shift to leave the stress effect. This was the approach taken in two recent papers [66, 67] regarding stress measurement in polycrystalline alumina. It was emphasized in those papers and elsewhere that the corrections of Eq. (1a) and the selection of the correct proportionality constants—the coefficients—are critical in accurate and precise stress measurement [2, 136]. It is the experimental determination of these coefficients that is the subject of this review. The review has several goals: (1) to provide historical context for the coefficients, so that prior work can be judged in terms of new results; (2) to guide selection of the “right” coefficients and, where possible, their accuracy and precision; (3) to guide against wrongly cited or attributed coefficients; (4) to provide (in one place, with common notation) simple relations for common geometries to show how the coefficients are used, including for polycrystals; and (5) to assess the importance of temperature and composition corrections.

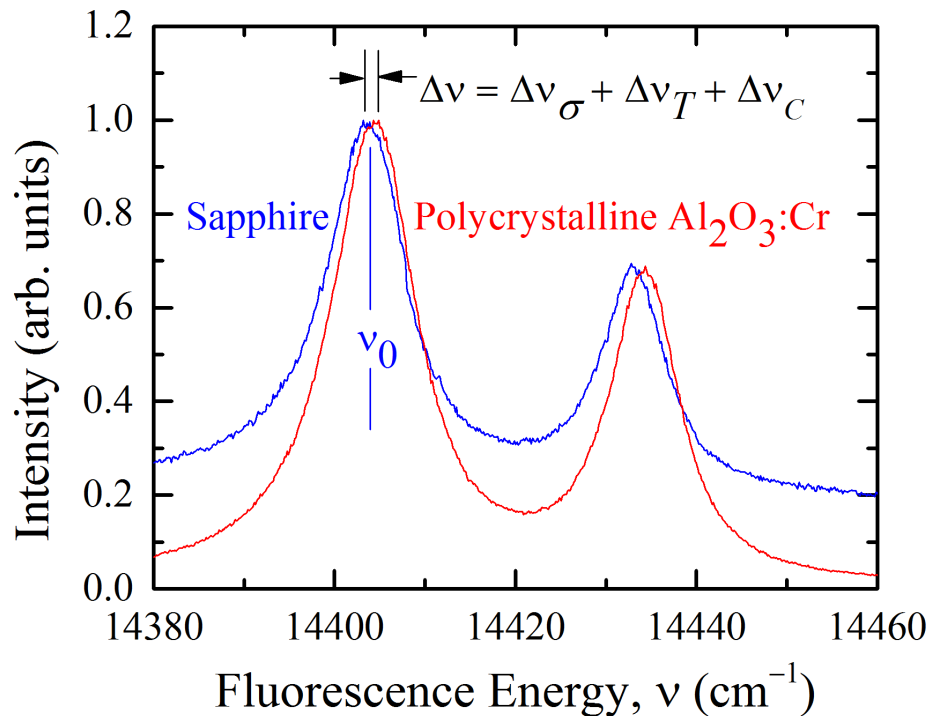


Fig. 6. Fluorescence spectra for sapphire and polycrystalline Al₂O₃, showing the R₁ and R₂ peaks and the notation for peak shift due to stress, temperature, and composition effects. This review emphasizes that the use of the correct coefficients can relate the shifts to stress in the Al₂O₃ structure.

2. Background Analysis

This section defines the coefficients that linearly relate the changes in energy of the ruby R lines to the imposition of stress, changes in temperature, and changes in (Cr) composition of a material. The importance of knowledge of the values of the coefficients (and their uncertainties), which is the focus of the review and the next section, is made clear. The section begins with an analysis of the stress coefficients before moving on to the simpler temperature and composition coefficients.

2.1 Stress

The linear analysis relating the scalar shift in energy, $\Delta\nu_\sigma$, due to stress effects alone and the stress tensor acting within a ruby single crystal, σ_{ij}^* , begins with the equation first given by Grabner [38]:

$$\Delta\nu_\sigma = \Pi_{ij}\sigma_{ij}^*. \quad (2)$$

Here, σ_{ij}^* is defined relative to the crystal coordinate system (denoted by the superscript star, *), as is the stress-optical or piezospectroscopic tensor Π_{ij} . The indices i, j each take the values 1, 2, 3, corresponding to a, m, c here. The Einstein summation convention is assumed throughout. The piezospectroscopic tensor is assumed to have the same (trigonal) symmetry as the ruby lattice (D_{3d}), and consequently the off-diagonal components of the (symmetric, second rank) tensor are zero in the crystal coordinate system. The piezospectroscopic tensor is thus

$$\Pi_{ij} = \begin{bmatrix} \Pi_{11} & 0 & 0 \\ 0 & \Pi_{22} & 0 \\ 0 & 0 & \Pi_{33} \end{bmatrix}, \quad (3)$$

and Eq. (2) reduces to

$$\begin{aligned} \Delta\nu_\sigma &= \Pi_{11}\sigma_{11}^* + \Pi_{22}\sigma_{22}^* + \Pi_{33}\sigma_{33}^* \\ &= \Pi_a(\sigma_{11}^* + \sigma_{22}^*) + \Pi_c\sigma_{33}^*. \end{aligned} \quad (4)$$

Two further reductions are possible, one empirical (and very useful) and the other mathematical (and even more useful). The first reduction is that, empirically, $\Pi_{11} = \Pi_{22}$, implying that the piezospectroscopic effect is uniform perpendicular to the crystal axis and takes on the a -axis value (similar to elastic and thermal expansion effects). Hence, the notation $\Pi_{11} = \Pi_{22} = \Pi_a$ is used; the remaining component is designated $\Pi_{33} = \Pi_c$; see the second line of Eq. (4). The second reduction is to note that under hydrostatic compressive loading conditions, the three stress components are equal, $\sigma_{11}^* = \sigma_{22}^* = \sigma_{33}^* = -p$, where p is the pressure. Thus, Eq. (4) becomes the scalar equation

$$p = -\Delta\nu_p/\Pi_p = -\Delta\nu_p/(2\Pi_a + \Pi_c), \quad (5)$$

which is the basis (when calibrated [16, 20, 21, 25]) for ruby pressure measurement in the DAC and other high-pressure experiments, and which provides insight into the origin of the pressure proportionality constant $\Pi_p = (2\Pi_a + \Pi_c)$. Both Π_a and Π_c are usually positive and hence pressure decreases the fluorescence energy (or increases the wavelength of the fluorescent light [16, 20]).

Note that a crystal need not be aligned with the x - y - z coordinate system of the sample or laboratory frame (particularly true in polycrystals, but irrelevant in DAC experiments as the pressure field is frame invariant). Note also that the (off-diagonal) shear stresses in the crystal frame are not necessarily zero or assumed to be zero (i.e., that $\sigma_{ij}^* = 0, i \neq j$ is not necessarily true or assumed), just that the energy shift in Eq. (4) is not sensitive to them. These two concepts can be put together by relating the stress applied in the sample or laboratory (or arbitrary) frame (σ_{mn} , no star) to that appearing in the (starred) crystal frame,

$$\sigma_{ij}^* = a_{im} a_{jn} \sigma_{mn}, \quad (6)$$

where a_{ij} is the orthogonal transformation matrix relating the two frames [137] (and is frequently the product of three rotation matrices based on Euler angles [43]). Combining Eqs. (2), (3), and (6), the empirical equality $\Pi_{11} = \Pi_{22}$, and the tensor identity $a_{ij} a_{ik} = \delta_{jk}$, where δ_{jk} is the Krönecker delta, leads to a general expression for the energy shift for a crystal set in a sample or laboratory frame [43],

$$\begin{aligned} \Delta v_\sigma &= \Pi_a(\sigma_{11} + \sigma_{22} + \sigma_{33}) + (\Pi_c - \Pi_a)(a_{31}^2 \sigma_{11} + a_{32}^2 \sigma_{22} + a_{33}^2 \sigma_{33}) \\ &\quad + 2(\Pi_c - \Pi_a)(a_{31} a_{32} \sigma_{12} + a_{32} a_{33} \sigma_{23} + a_{31} a_{33} \sigma_{31}) \\ &= \Pi_a \sigma_{ii} + (\Pi_c - \Pi_a) a_{3i} a_{3j} \sigma_{ij}. \end{aligned} \quad (7)$$

Equation (7) makes clear the role in the sample or laboratory frame of shear stresses and off-diagonal transformation terms. Equation (7) also makes clear that with the assumption $\Pi_{11} = \Pi_{22} = \Pi_a$, Eq. (7) is just a recasting of Eq. (4): There are still only two piezospectroscopic degrees of freedom. In the pressure equation, Eq. (5), which assumes hydrostatic loading, there is only one piezospectroscopic degree of freedom. Equation (7) is also useful because it provides the fluorescence energy shift when the orientation of the crystal is known in the sample or laboratory frame, and hence a_{ij} is known. Such an orientation might be known from X-ray diffraction or electron backscatter diffraction [138] measurements or from prior knowledge of the material, e.g., a polycrystal in which the grain orientations, and hence the a_{ij} values, are distributed randomly [43]. Combining Eq. (7) with the specification of a hydrostatic field, $\sigma_{ij} = -p \delta_{ij}$, and the tensor identity $a_{ij} a_{kj} = \delta_{ik}$ recovers the pressure equation, Eq. (5), showing that the pressure response is indeed frame independent.

Equations (2) and (3) can be combined in a different way, again using the empirical equality $\Pi_{11} = \Pi_{22}$, to give

$$\begin{aligned} \Delta v_\sigma &= \frac{(2\Pi_a + \Pi_c)(\sigma_{11}^* + \sigma_{22}^* + \sigma_{33}^*)}{3} + \frac{(\Pi_c - \Pi_a)(2\sigma_{33}^* - \sigma_{11}^* - \sigma_{22}^*)}{3} \\ &= (2\Pi_a + \Pi_c)\sigma_M + (\Pi_c - \Pi_a)\sigma_S, \end{aligned} \quad (8)$$

where the second line emphasizes that the shift in energy arises from a mean stress contribution (σ_M) plus a shear stress contribution (σ_S) [67]:

$$\sigma_M = (\sigma_{11}^* + \sigma_{22}^* + \sigma_{33}^*)/3, \quad (9a)$$

$$\sigma_S = (2\sigma_{33}^* - \sigma_{11}^* - \sigma_{22}^*)/3. \quad (9b)$$

It should be recognized that the preceding equations, i.e., Eqs. (1–5), (7), and (8), apply to each of the R_1 and R_2 lines separately. Hence, the coefficients for the stresses in Eq. (8) are strictly defined as

$$\Pi_M^{(1)} = (2\Pi_a^{(1)} + \Pi_c^{(1)}), \quad (10a)$$

$$\Pi_S^{(1)} = (\Pi_c^{(1)} - \Pi_a^{(1)}), \quad (10b)$$

$$\Pi_M^{(2)} = (2\Pi_a^{(2)} + \Pi_c^{(2)}), \quad (10c)$$

$$\Pi_S^{(2)} = (\Pi_c^{(2)} - \Pi_a^{(2)}), \quad (10d)$$

where the superscript labels ⁽¹⁾ and ⁽²⁾ here and throughout indicate parameters associated with the R_1 and R_2 lines, respectively. Equation (10) enables Eq. (8) to be written compactly in matrix form for each fluorescent line:

$$\begin{bmatrix} \Delta\nu^{(1)} \\ \Delta\nu^{(2)} \end{bmatrix} = \begin{bmatrix} \Pi_M^{(1)} & \Pi_S^{(1)} \\ \Pi_M^{(2)} & \Pi_S^{(2)} \end{bmatrix} \begin{bmatrix} \sigma_M \\ \sigma_S \end{bmatrix}, \quad (11a)$$

noting that there are still only two piezospectroscopic degrees of freedom (for each shift). Consequently, two components of the stress field (σ_M, σ_S) in the crystallographic frame can be specified through inversion of Eq. (11a) to

$$\begin{bmatrix} \sigma_M \\ \sigma_S \end{bmatrix} = (\Pi_M^{(1)}\Pi_S^{(2)} - \Pi_S^{(1)}\Pi_M^{(2)})^{-1} \begin{bmatrix} \Pi_S^{(2)} & -\Pi_S^{(1)} \\ -\Pi_M^{(2)} & \Pi_M^{(1)} \end{bmatrix} \begin{bmatrix} \Delta\nu^{(1)} \\ \Delta\nu^{(2)} \end{bmatrix}, \quad (11b)$$

using the two energy shift measurements ($\Delta\nu^{(1)}, \Delta\nu^{(2)}$). A similar analysis can be applied if the stress field in the crystallographic coordinates is assumed to be rotationally invariant perpendicular to the c axis, such that only two stress components in the crystallographic frame need be specified, $\sigma_{11}^* = \sigma_{22}^* = \sigma_a$ and $\sigma_{33}^* = \sigma_c$. Equation (4) can then be written and inverted as Eq. (11).

Finally, Eqs. (4) and (6) can be combined to give the shift in the sample or laboratory frame, *averaged* over a large number of randomly oriented grains:

$$\overline{\Delta\nu_\sigma} = \left(\frac{1}{3}\right) \Pi_{ii} \overline{\sigma_{jj}} = \left(\frac{1}{3}\right) (\Pi_{11} + \Pi_{22} + \Pi_{33}) (\overline{\sigma_{11}} + \overline{\sigma_{22}} + \overline{\sigma_{33}}), \quad (12)$$

where the overbar indicates an ensemble average, and the averages $\overline{a_{ij}^2} = 1/3$ and $\overline{a_{ij}a_{ik}} = 0$, where $j \neq k$ [43], have been used. There is only one piezospectroscopic degree of freedom as the assumption of a random collection of grains has been made in deriving Eq. (12). One of the simplest examples is the simple bending of a polycrystalline beam, in which the fluorescent measurement encompasses many grains [42]. In this case, $\sigma_{11} = \sigma_u = Mz/I$, and $\sigma_{22} = \sigma_{33} = 0$, where M here is the bending moment applied to the beam, I is the beam moment of inertia, z is the distance from the neutral axis, and σ_u is the resulting uniaxial stress at z . Another simple example is the biaxial stressing of a polycrystalline film on a thermal expansion mismatched substrate, in which again the fluorescence measurements encompass many grains [96]. Here, $\sigma_{11} = \sigma_{22} = \sigma_b$, and $\sigma_{33} = 0$, where σ_b is the film-substrate mismatch imposed biaxial stress. In the first case,

$$\overline{\Delta\nu_\sigma} = \left(\frac{1}{3}\right) (2\Pi_a + \Pi_c) \sigma_u$$

and in the second,

$$\overline{\Delta\nu_\sigma} = \left(\frac{2}{3}\right) (2\Pi_a + \Pi_c) \sigma_b.$$

Both equations apply separately to the R₁ and R₂ lines, although, as will be seen, experimentally the distinction between the lines is not meaningful. The similarity of these equations to the pressure relation, Eq. (5), is clear.

2.2 Temperature and Composition

The shifts in the R-line fluorescence energy with temperature and composition in typical measurements on alumina are simple proportionalities. The shift with temperature, T (K), is given by

$$\Delta\nu_T = \beta_T (T - T_{\text{ref}}), \quad (13)$$

where T_{ref} is a reference temperature (taken as 298.8 K, following Munro [135]), and β_T is the proportionality coefficient. Under normal circumstances, β_T is negative, such that the fluorescence energy decreases with increasing temperature (see Fig. 5).

The shift with composition, C , is given by a relation similar to Eq. (13) but with no reference point:

$$\Delta\nu_C = \beta_C C, \quad (14)$$

where C is the Cr composition given by the mass fraction (not percentage [139]) of Cr in the $\text{Al}_2\text{O}_3:\text{Cr}$ structure [66]. β_C is positive, such that fluorescence energy increases with Cr content. Both β_T and β_C are different for the R_1 and R_2 lines.

Although not exhaustive, the applications mentioned in the Introduction and the formulae presented in this analysis section should make clear that measurement of the energies of the R_1 and R_2 fluorescent lines in alumina provides a powerful method for noncontact local measurement of stress. It should be equally clear that the accuracy and precision of such measurements depend on knowledge of the coefficients Π_a , Π_c , β_T , and β_C for each line. The following section, which is the focus of the review, examines the experimental development of the numerical values of these coefficients.

3. Coefficient Measurements

Despite the 65 year period spanned by the papers covered in this review, the many instruments used to measure the coefficients reviewed here were broadly similar in basic functionality. Each instrument utilized a visible light source for excitation of the Cr^{3+} fluorescence and high-resolution dispersive detection for measuring the precise energy of the R_1 and R_2 fluorescence transitions. Early measurements utilized lamp and filter combinations for excitation (e.g., Ref. [140]); by the early 1980s, visible lasers had replaced the lamp sources [23]. Spectral measurements were typically made with a scanning grating monochromator with a single element detector, until parallel spectral detection schemes with diode arrays or charged coupled devices became common in the late 1990s [141]. Each instrument also employed a cell for mounting the alumina specimen in a specific geometry with a means for controlling the external applied stress and the temperature. The majority of instruments used microscope objective lenses of modest magnification (e.g., $10\times$) for both the excitation and detection of fluorescence in both transmitted light and reflection (as in Figs. 3, 4, 6) geometries, yielding spot sizes in the tens of micrometers. A typical implementation of these instrumental features consisted of a DAC mounted in an upright optical microscope coupled to a grating monochromator. Barnett and coworkers presented a detailed description of this type of system [17].

3.1 Hydrostatic Pressure Loading

The measurements of the energy changes of the ruby R-lines with hydrostatic pressure provide not only useful qualitative background for uniaxial stress measurements (next section), but quantitative constraints that the uniaxial measurements must meet. Qualitatively, hydrostatic measurements are simple to understand and compare, Eq. (5) is scalar, and provide a measure of the effect. Quantitatively, hydrostatic measurements provide a pressure coefficient that constrains the sum of the uniaxial coefficients, via Eq. (5).

Table 1 gives the first author, year published, citation, R-line coefficients (R_1 or R_2), and notes for original works that (experimentally) determined the pressure coefficients in Eq. (5), $\Pi_p^{(1)}$ and $\Pi_p^{(2)}$, directly. Where necessary, the coefficients have been converted to a common set of units ($\text{cm}^{-1}/\text{GPa}$). In the linear, low-pressure range, the coefficient was often given as

$$\Delta\lambda/\Delta p,$$

where λ is the wavelength of the fluorescence. It is easy to show (using $\lambda \sim 1/\nu$) that

$$\frac{\Delta\nu}{\Delta p} = \Pi_p = -\frac{1}{\lambda^2} \frac{\Delta\lambda}{\Delta p}$$

and calculate the coefficient using $\lambda = \lambda_0$, where λ_0 is the wavelength of an unaffected system (here 694.24 nm). In the full, nonlinear range, including high pressure, the variation is often given in the form proposed by Mao *et al.* [25],

$$p = \left(\frac{A}{B}\right) \left[\left(\frac{\Delta\lambda}{\lambda_0}\right)^B - 1 \right],$$

where A and B are empirical fitting parameters. This equation can be inverted to give (as used in Fig. 5)

$$\frac{\Delta\nu}{\nu_0} = \left[p \left(\frac{B}{A}\right) + 1 \right]^{(-\frac{1}{B})} - 1,$$

which, in the low-pressure limit, reverts to

$$\frac{\Delta\nu}{\Delta p} = \Pi_p = \frac{\nu_0}{A}$$

to calculate the coefficient. A dash in Table 1 indicates a coefficient was not specified. Where not given, uncertainties were not specified. Uncertainties in parentheses ($\pm x$) represent an estimate based on information given in the publication. Otherwise, unless noted, uncertainties are those specified in the publication and represent standard deviations of the means of experimental measurements. Most determinations used DAC measurements. The pressures given are those up to which the authors observed a linear variation of fluorescence shift with pressure and reported a coefficient, although, in some cases, linear behavior to greater pressures (a few tens of gigapascals) [16, 17, 20] was observed. The term “extrapolated” implies that observations were made over the full pressure range, including high pressure, and extrapolated into the low-pressure range to obtain a coefficient. As noted by Chijoike [34], this linear, low-pressure range extends experimentally up to many tens of gigapascals.

Table 1. Pressure coefficients for R-line shifts in alumina.

Author	Coefficient, $\Pi_p^{(1)}$ (cm ⁻¹ /GPa)	Coefficient, $\Pi_p^{(2)}$ (cm ⁻¹ /GPa)	Notes
Paetzold, 1951 [142] pressure up to 0.1 GPa	9.4	8.3	290 K
Langer, 1967 [143] pressure up to 1 GPa	9.0 ± 0.5	9.0 ± 0.5	
Forman, 1972 [16] pressure up to 2.2 GPa	7.7 ± 0.3	8.4 ± 0.3	
Barnett, 1973 [17] pressure up to 10 GPa	$7.5 (\pm 0.4)$	$7.5 (\pm 0.4)$	“accurate to approximately 10 %”
Piermarini, 1975 [20] pressure up to 19.5 GPa	7.572 ± 0.044	—	“95 % confidence interval”
Adams, 1976 [21] pressure up to 5 GPa	7.3 ± 0.2	7.3 ± 0.2	166.8 K
Mao, 1978 [22]	$7.57 (\pm 0.45)$	—	extrapolated from fit function “total random error ... $\pm 6 \%$ ”
Munro, 1985 [135] pressure up to 14.5 GPa	7.59 ± 0.04	7.615 ± 0.004	“99 % confidence level”
Mao, 1986 [25]	7.56	—	extrapolated from fit function
Eggert, 1989 [26]	7.6	7.6	extrapolated from graph
Ragan, 1996 [144] pressure up to ~15 GPa	7.6	—	
He, 1999 [88] pressure up to 5 GPa	7.65	7.56	polycrystal
Grasset, 2001 [136] pressure up to 1 GPa	$7.68 (\pm 0.15)$	$7.79 (\pm 0.15)$	95 % confidence interval
Chijoike, 2005, Silvera 2007 [34, 35]	7.678 ± 0.027	7.678 ± 0.027	extrapolated from fit function

Table 1 shows that the initial measurements of Π_p were probably overestimates, that the accepted value, about $7.6 \text{ cm}^{-1}/\text{GPa}$, was established in the 1970s, and that the effect of hydrostatic pressure was the same for both R_1 and R_2 (i.e., $\Pi_p^{(1)} = \Pi_p^{(2)}$). In fact, this last observation is now taken as an indication of pure hydrostatic (i.e., zero shear) loading in high-pressure DAC experiments that make use of Eq. (5) in determining pressure [34]. The overall (between-laboratory) uncertainty in Π_p can be estimated from Table 1 as about $0.07 \text{ cm}^{-1}/\text{GPa}$, and this is consistent with the total variation (about $0.14 \text{ cm}^{-1}/\text{GPa}$) of mean “A” values in two compilations [2, 145] of high-pressure measurements. (The values quoted here are representative of the historical variability and are not the result of statistical calculation.) On a practical note, the information in Table 1 states that the numerical proportionality relationships for energy shift in a random polycrystal under uniaxial stress, equibiaxial stress, and equitriaxial stress (negative pressure) (in the ratios 1/3:2/3:1, see above) are $\sigma_u = \Delta\nu_\sigma/2.5$, $\sigma_b = \Delta\nu_\sigma/5.1$, and $p = -\Delta\nu_\sigma/7.6$.

3.2 Uniaxial Stress Loading

3.2.1 Quasi-Static Tests

Table 2. Stress coefficients^a for R-line shifts in alumina.

Author	$\Pi_a^{(1)}$	$\Pi_m^{(1)}$	$\Pi_c^{(1)}$	Inferred Pressure Coefficient, $\Pi_p^{(1)}$	$\Pi_a^{(2)}$	$\Pi_m^{(2)}$	$\Pi_c^{(2)}$	Inferred Pressure Coefficient, $\Pi_p^{(2)}$
Schawlow, 1961 [140] stress to -0.1 GPa	3.07 ± 0.07	—	1.83 ± 0.01	7.97 ± 0.14	2.75 ± 0.04	—	2.35 ± 0.03	7.85 ± 0.09
Kaplyanskii, 1962 [146] stress unknown	3.1		1.4	7.6	2.7		1.9	7.3
Sturge, 1965 [147] stress unknown							$\Pi_c^{(1)} + 0.57 \pm 0.04$	
Feher, 1968 [148] stress to -0.9 GPa	2.8 ± 0.1 2.70 ± 0.04	2.6 ± 0.2	2.15 ± 0.1 1.83 ± 0.03	7.23 ± 0.09	2.8 ± 0.1 2.28 ± 0.02	2.6 ± 0.2	2.15 ± 0.1 2.38 ± 0.03	6.94 ± 0.05
Fujishiro, 1988 [149] stress to -1.2 GPa	2.939 ± 0.041		1.616 ± 0.066	7.49 ± 0.09	2.062 ± 0.102		2.112 ± 0.094	6.24 ± 0.17
He, 1995 [45] stress to -0.9 GPa	2.56 3.12 ± 0.04	3.5 3.40 ± 0.01	1.53 1.55 ± 0.02	7.59 8.07 ± 0.05	2.65 2.66 ± 0.02	2.80 2.81 ± 0.02	2.16 2.22 ± 0.02	7.61 7.69 ± 0.03
<i>Mean</i>	2.87 ± 0.06	2.95 ± 0.55	1.65 ± 0.04	7.67 ± 0.11	2.49 ± 0.07	2.70 ± 0.10	2.19 ± 0.07	7.20 ± 0.12
<i>Constrained Values</i>	2.98	—	1.64	7.60	2.64	—	2.32	7.60

^aAll coefficients are given in ($\text{cm}^{-1}/\text{GPa}$).

Table 2 gives the first author, year published, citation, and R-line coefficients (R_1 or R_2) for original works that (experimentally) determined the stress coefficients for different crystal orientations, $\Pi_a^{(1)}$, $\Pi_m^{(1)}$, and $\Pi_c^{(1)}$ and $\Pi_a^{(2)}$, $\Pi_m^{(2)}$, and $\Pi_c^{(2)}$, directly; see Eq. (4). Allowance is made for the possibility $\Pi_m^{(x)} \neq \Pi_a^{(x)}$ where such measurements were made. Values in bold font indicate specification in the original publication. The compressive stresses given are those to which the authors observed a linear variation of fluorescence shift with stress and reported a coefficient. A dash indicates a coefficient was not specified. Where not given, uncertainties were not specified. Where necessary, the coefficients have been converted to a common set of units ($\text{cm}^{-1}/\text{GPa}$). Values in regular font indicate coefficients and their uncertainties (standard deviations of fitting parameters) determined from digitizing and linear best-fitting data provided in graphical form in original publications. The inferred pressure coefficients were determined from $\Pi_p^{(x)} = \Pi_a^{(x)} + \Pi_m^{(x)} + \Pi_c^{(x)}$ or $\Pi_p^{(x)} = 2\Pi_a^{(x)} + \Pi_c^{(x)}$, Eqs. (4) and (5); uncertainties (standard deviations) for the

$\Pi_p^{(x)}$ values were determined by summing uncertainties from the individual coefficients in quadrature. That is, the uncertainty in Π_p , $u(p) = [u^2(\Pi_a) + u^2(\Pi_m) + u^2(\Pi_c)]^{1/2}$, and so forth, where $u(\Pi_i)$ is the uncertainty in a single coefficient. Mean values were determined by averaging the observed coefficients in each column. Uncertainties (standard deviations) for the mean values were determined by summing uncertainties from the column coefficients in quadrature (as stated). The *mean* values and uncertainties reflect the broad observations and are for ease of comparison only, and no distinction was made between column parameters. The *constrained* values reflect the two-parameter constraint sum of Eq. (5) and the experimental observations of Table 1; the observed mean $\Pi_c^{(x)}$ values were multiplied by the ratio of the observed mean inferred $\Pi_p^{(x)}$ values/7.60, and the $\Pi_a^{(x)}$ values were adjusted accordingly to meet the constraint of Eq. (5).

The stress coefficients of Table 2 display a much weaker historical variation (larger to smaller values) than the pressure coefficients of Table 1, reflecting more modern measurements. The calculated *mean* values thus provide the following broad trends: The pressure coefficients inferred from the uniaxial stress measurements are very close to those observed in hydrostatic tests (about $7.6 \text{ cm}^{-1}/\text{GPa}$); the $\Pi_a^{(x)}$ values are greater than the $\Pi_c^{(x)}$ values, though more so for the R_1 peaks (nearly a factor of two) than the R_2 peaks (nearly equal); where measured, the $\Pi_m^{(x)}$ values are greater than the $\Pi_a^{(x)}$ values, although this observation is barely significant; and, based on the first and last observations, the *constrained values* of the $\Pi_a^{(x)}$ and $\Pi_c^{(x)}$ coefficients are a faithful representation of all the observations. Within experimental uncertainty, the off-diagonal terms $\Pi_{12} = \Pi_{23} = \Pi_{31} = 0$ [45], consistent with Eq. (3). (The discrepancies between some published and digitized values in Table 2, e.g., $\Pi_a^{(1)}$ from Ref. [45], probably arise from fitting the data to a quadratic equation of the form $\Delta v = c_1\sigma + c_2\sigma^2$ and publishing c_1 as Π . This is incorrect within the spirit of the analysis and inconsistent with measurements over a broad pressure range in which nonlinearity only appears at very high pressures, e.g., Fig. 5. Uniaxial measurements were typically at peak stress levels, about 1 GPa, about two orders of magnitude less than the peak pressure levels in hydrostatic measurements, about 100 GPa, in which nonlinear effects are still small [34]. The single observation in one uniaxial study might have exhibited nonlinearity, but the small stress level, ~ 0.4 GPa, suggests it was probably due to fixture compliance; the observation is unverified. Again, on a practical note, the information in Table 2 states that the numerical proportionality relationships for energy shift in an unconstrained single-crystal *c*-axis fiber under uniaxial stress are $\sigma_u = \Delta v_\sigma^{(1)}/1.6$ and $\sigma_u = \Delta v_\sigma^{(2)}/2.3$.

3.2.2 Shock Tests

The values in Tables 1 and 2 were obtained from quasi-static tests. Values obtained from rapid, shock-loading tests by Gupta, Sharma, and colleagues agree with those in Tables 1 and 2, but some care is required in comparisons. First, although cast as uniaxial tests, the shock tests had mixed loading, i.e., neither uniaxial nor hydrostatic. The samples were *c*- or *a*-oriented single crystals, with much of the loading (σ_{33} in the laboratory frame) more than 10 GPa, generating substantial σ_{11}^* or σ_{33}^* longitudinal stresses, respectively [150, 151]. However, the shock-loading geometry also generated substantial simultaneous *lateral* stresses (σ_{11} and σ_{22})—up to 24 % of the longitudinal stress in the case of the *c* crystal [151] (generating similarly large σ_{11}^* and σ_{22}^*) and up to 77 % in the case of the *a* crystal [150] (large σ_{22}^* and σ_{33}^*). A nonlinear third-order stress analysis was used to calculate the stress values [150]; the stress analysis was unverified. Second, comparisons between the quasi-static and shock experiments were made by calculating the change in energies of the *R* lines as a function of relative volume change (dilatational strain) under *hydrostatic* and shock loads using a nonlinear (Murnaghan), but *isotropic*, bulk modulus; the volume or density change using this nonlinear modulus assumption was unverified. Consistency with the referenced $7.6 \text{ cm}^{-1}/\text{GPa}$ hydrostatic pressure sensitivity [135] was shown, almost ideally so in the case of the *a* crystal, which had a greater hydrostatic component, but no uncertainty measure was provided for the data. The origin of the slight nonlinearity observed in some of the data is unknown given the unverified analysis methods.

3.2.3 Fiber Tests

True uniaxial tensile measurements (up to 0.8 GPa) were performed in early experiments by Liu *et al.* [79] on a free fiber stated to be single crystal, but which contained twins with c axes at an angle of 20° to 30° to the fiber axis (and thus σ_{33}^* was similarly misaligned with the applied stress σ_{33}). Values in the laboratory 3-direction of $\Pi_{\text{twinned}}^{(1)} \approx 1.7 \text{ cm}^{-1}/\text{GPa}$ and $\Pi_{\text{twinned}}^{(2)} \approx 2.3 \text{ cm}^{-1}/\text{GPa}$ were demonstrated, and consistency was claimed with the published values of Feher and Sturge [148]. (The fiber values were in fact more consistent with the smaller-value independent data fits to Ref. [148]; see Table 2.) Tests (up to 1.7 GPa) on single-crystal sapphire filaments bound in an epoxy matrix with the crystal c -axis aligned with the filament axis gave $\Pi_c^{(1)} = 1.31 \text{ cm}^{-1}/\text{GPa}$ and $\Pi_c^{(2)} = 1.90 \text{ cm}^{-1}/\text{GPa}$ [86, 91], which are somewhat smaller than the consensus values (Table 2). Subsequent tests [89] on single-crystal fibers under uniaxial tension and compression (3-tensile axis aligned with c axis, stress magnitude up to 0.55 GPa) gave a R_2 shift of $877 \text{ cm}^{-1}/\text{strain} \pm 82 \text{ cm}^{-1}/\text{strain}$, which, in concert with the Young's modulus of $411 \text{ GPa} \pm 24 \text{ GPa}$, produced $\Pi_c^{(2)} = 2.13 \text{ cm}^{-1}/\text{GPa} \pm 0.23 \text{ cm}^{-1}/\text{GPa}$, a value more consistent with the consensus value (Table 2).

Experimental measurements on free $80\text{Al}_2\text{O}_3\text{-}20\text{ZrO}_2$ polycrystalline composite fibers under uniaxial tension (up to 1.8 GPa) were reported by Yang and Young [82, 83]. These measurements gave sensitivities of $610 \text{ cm}^{-1}/\text{strain}$ and $700 \text{ cm}^{-1}/\text{strain}$ for R_1 and R_2 , respectively, which, combined with the Young's modulus of 254 GPa, give $\Pi_{\text{poly}}^{(1)} = 2.4 \text{ cm}^{-1}/\text{GPa}$ and $\Pi_{\text{poly}}^{(2)} = 2.8 \text{ cm}^{-1}/\text{GPa}$. These values, as noted by the authors, are consistent with the predicted random polycrystalline response under uniaxial loading of $(7.6/3) \text{ cm}^{-1}/\text{GPa} = 2.5 \text{ cm}^{-1}/\text{GPa}$ from Eq. (12). Measurements in which an $80\text{Al}_2\text{O}_3\text{-}20\text{ZrO}_2$ fiber was fixed to a (presumably constraining) substrate [84] gave $2.9 \text{ cm}^{-1}/\text{GPa}$.

Measurements on a polycrystalline, single-phase $\alpha\text{-Al}_2\text{O}_3$ fiber fixed to a substrate gave 1330 $\text{cm}^{-1}/\text{strain}$, and using the greater Young's modulus value of 380 GPa gave a (probably constrained) value of $\Pi_{\text{poly}}^{(2)} = 3.5 \text{ cm}^{-1}/\text{GPa}$ [87]. Uniaxial tensile measurements on a (presumably free, but constraint unstated) similar polycrystalline $\alpha\text{-Al}_2\text{O}_3$ fiber gave $\Pi_{\text{poly}}^{(2)} = 2.53 \text{ cm}^{-1}/\text{GPa}$, noted to be consistent with the predicted polycrystalline response under uniaxial loading; see previous paragraph and Eq. (12) [88]. Uniaxial tension and compression tests [89] on a polycrystalline $\alpha\text{-Al}_2\text{O}_3$ fiber gave a R_2 shift of $1178 \text{ cm}^{-1}/\text{strain} \pm 54 \text{ cm}^{-1}/\text{strain}$, and using a modulus of $375 \text{ GPa} \pm 5 \text{ GPa}$ gave $\Pi_{\text{poly}}^{(2)} = 3.14 \text{ cm}^{-1}/\text{GPa} \pm 0.14 \text{ cm}^{-1}/\text{GPa}$, which is larger than the predicted polycrystalline response. Similar tests (up to 2 GPa) on a similar fiber [90] gave $799 \text{ cm}^{-1}/\text{strain}$ and $757 \text{ cm}^{-1}/\text{strain}$ for R_1 and R_2 , respectively, which, using the (manufacture) cited modulus of 260 GPa, give $\Pi_{\text{poly}}^{(1)} = 3.07 \text{ cm}^{-1}/\text{GPa}$ and $\Pi_{\text{poly}}^{(2)} = 2.91 \text{ cm}^{-1}/\text{GPa}$, which are larger than the predicted polycrystalline response.

In many fiber tests [79, 82, 83, 86, 90, 91], extensive data were provided to characterize the shift in the fluorescence energy with applied stress or strain. The stress or strain were extremely simple to determine given the extremely simple (fiber) geometry; in the case of uniaxial strain measurements, the conjugate uniaxial stress was easily calculated *via* a simple, linear plane-stress Young's modulus. Hence, the linear variation of shift with applied stress (up to a few gigapascals) is well verified by many observations with no caveats. The numerical agreement with the nonfiber coefficient determinations surveyed above further supports the observations.

3.2.4 Bulk Polycrystal Tests

There appear to be very few experimental measurements of piezospectroscopic effects in bulk polycrystals under uniaxial loading. Molis and Clarke [42] measured the R_1 fluorescence energy shifts, importantly in compression *and* tension, in a polycrystalline beam in bending experiments (stress range $\pm 0.17 \text{ GPa}$), obtaining $\Pi_{\text{poly}}^{(1)} = 2.4 \text{ cm}^{-1}/\text{GPa} \pm 0.1 \text{ cm}^{-1}/\text{GPa}$. Similar bending experiments (stress range $\pm 0.25 \text{ GPa}$) on a polycrystalline material were performed by Ma and Clarke [43], obtaining $\Pi_{\text{poly}}^{(1)} = 2.46 \text{ cm}^{-1}/\text{GPa}$ and $\Pi_{\text{poly}}^{(2)} = 2.50 \text{ cm}^{-1}/\text{GPa}$. Extending their fiber experiments, Dassios and Galiotis [90] tested

bulk polycrystals under uniaxial compression (stress to -0.15 GPa) and obtained $\Pi_{\text{poly}}^{(1)} = 2.57 \text{ cm}^{-1}/\text{GPa} \pm 0.03 \text{ cm}^{-1}/\text{GPa}$ and $\Pi_{\text{poly}}^{(2)} = 2.52 \text{ cm}^{-1}/\text{GPa} \pm 0.03 \text{ cm}^{-1}/\text{GPa}$. Margueron and Clarke [115] tested thin-film polycrystals under uniaxial tension and compression (stress range ± 4 GPa, later changed to -8 GPa to 0 GPa [58]) and obtained $\Pi_{\text{poly}}^{(2)} = 2.50 \text{ cm}^{-1}/\text{GPa} \pm 0.03 \text{ cm}^{-1}/\text{GPa}$. The R_1 data were similar but exhibited slightly different coefficients in tension and compression. The observation (especially the strain gauge measurements) was unverified. All the above measurements agree with the polycrystalline prediction for uniaxial loading of $2.5 \text{ cm}^{-1}/\text{GPa}$ from Eq. (12). As with the fiber tests, extensive data were provided for the polycrystals to characterize the shift in fluorescence energy with stress or strain, where the stress or strain were extremely simple to determine given the simple (bending or compression) geometries, and the stress was easily calculated from strain *via* a Young's modulus. Hence, the linear variation of shift with applied stress (up to a few hundred megapascals; one unverified exception) and the numerical agreement with the non-polycrystal coefficient determinations surveyed above further support the observations. It is noted that the applied stress range of the polycrystal experiments was about an order of magnitude less than the single-crystal or fiber experiments (previous sections) and comparable to the intrinsic microstructural stresses expected and observed in bulk polycrystals [38–42, 58–67].

3.3 Temperature

Table 3 gives the first author, year published, citation, R-line coefficients (R_1 or R_2), and notes for original works that (experimentally) determined the temperature coefficients $\beta_T^{(1)}$ and $\beta_T^{(2)}$; see Eq. (13). Where necessary, the coefficients have been converted to a common set of units (cm^{-1}/K). A dash in Table 3 indicates a coefficient was not specified. Where not given, uncertainties were not specified. Uncertainties in parentheses ($\pm x$) represent an estimate based on information given in the publication. Otherwise, unless noted, uncertainties are those specified in the publication and represent standard deviations of the mean of experimental measurements.

A striking feature of Table 3 is that agreement regarding the value of the temperature coefficient of the R-line shifts in alumina (at 300 K) was achieved from the beginning: Most reported observations fall in the range $\beta_T^{(1)} = \beta_T^{(2)} = (-0.140 \pm 0.007) \text{ cm}^{-1}/\text{K}$, with no meaningful distinction between the behavior of R_1 and R_2 or meaningful historical variation. (The values quoted here are representative of the historical variability and are not the result of statistical calculation.)

3.4 Composition

There are extremely few reports of the effects of variations in the (dilute) Cr concentration on the energy shifts of the R lines in alumina or ruby. Dilute alumina or rubies are those in which isolated Cr ions do not interact quantum mechanically, but simply mechanically through the increased ionic volume of Cr^{3+} relative to Al^{3+} [1, 2, 44]. Early (and later) work showed that Cr ion pair interactions were very important in the optical properties of (heavily doped) ruby [61, 157–161], but such interactions are excluded here in consideration of piezospectroscopic effects in dilute ruby. Table 4 gives the first author, year published, citation, R-line coefficients (R_1 or R_2), and notes for original works that (experimentally) determined the composition coefficients $\beta_C^{(1)}$ and $\beta_C^{(2)}$; see Eq. (14). Where necessary, the coefficients have been converted to a common set of units ($\text{cm}^{-1}/\text{mass fraction Cr}$). A dash in Table 4 indicates a coefficient was not specified. Where not given, uncertainties were not specified. Uncertainties in parentheses ($\pm x$) represent an estimate based on information given in the publication. Otherwise, unless otherwise noted, uncertainties are those specified in the publication and represent standard deviations of the mean of experimental measurements.

Table 3. Temperature coefficients^a for R-line shifts in alumina.

Author	Coefficient, $\beta_T^{(1)}$ (cm ⁻¹ /K)	Coefficient, $\beta_T^{(2)}$ (cm ⁻¹ /K)	Notes
Paetzold, 1951 [142]	-0.139	-0.141	290 K
McCumber, 1963 [152]	-0.14 (± 0.02)	-0.14 (± 0.02)	interpolated from graph
Powell, 1966 [153]	-0.12 (± 0.02)	-0.12 (± 0.02)	interpolated from graph
Barnett, 1973 [17]	-0.14 (± 0.07)	-0.14 (± 0.07)	"accurate to approximately 10 %"
Yamaoka, 1980 [37]	-0.14	-	as cited by Ref. [29]
Wunder, 1981 [23]	-0.1487	-	"confidence level of >99 %"
Munro, 1985 [135]	-0.130 \pm 0.006	-0.122 \pm 0.006	"99 % confidence level"
Vos, 1991; Rekhi, 1999 [28, 32]	-0.136 (± 0.005)	-0.136 (± 0.005)	from R ₁ , R ₂ average fit equation; interpolated from graphs
Yen, 1992 [154]	-0.153	-	interpolated from graph
Ragan, 1992 [155]	-0.158	-0.162	linear approximation
Fujishiro, 1994 [29]	-0.133	-	
Huang, 1994 [156]	-0.140 (± 0.007)	-0.140 (± 0.007)	interpolated from graph
He, 1995 [45]	-0.144	-0.134	
Young, 1996 [83]	-0.167	-	interpolated from graph; composite fiber
Gibson, 1999 [141]	-0.133 (± 0.007)	-0.145 (± 0.007)	interpolated from graph
Grasset, 2001 [136]	-0.140 \pm 0.05	-0.137 \pm 0.05	95 % confidence interval
Kumari, 2011 [95]	-0.133	-0.133	interpolated from graph and empirical equation
Gao, 2015 [57]	-0.1519 \pm 0.0008	-0.1522 \pm 0.0014	0.556 % mass fraction of Cr sample

^aAll measurements were at approximately 300 K.

Table 4. Composition coefficients^a for R-line shifts in alumina.

Author	Coefficient, $\beta_C^{(1)}$ (cm ⁻¹ /mass fraction)	Coefficient, $\beta_C^{(2)}$ (cm ⁻¹ /mass fraction)	Notes
Kaplyanskii, 1969 [139]	96 \pm 5	101 \pm 5	77 K
Yu, 2002 [50]	-	82.7 and 136.4	RT ^b and 77 K
Gao, 2015 [57]	156 (± 50)	92 (± 20)	RT, estimated from graph
Michaels, 2016 [67]	160 (± 2)	167 (± 3)	RT
Margueron, 2017 [162]	100	100	

^aAll values in cm⁻¹/mass fraction of Cr in Al₂O₃ (i.e., 100 \times "wt %" of Cr in Al₂O₃:Cr [66]).

^bRT indicates room temperature.

Despite the few reported values (and caveats regarding the interfering effects of co-doping [50, 57]), a valid estimation (not a formal mean) seems to be $\beta_C^{(1)} = \beta_C^{(2)} \approx (120 \pm 30)$ cm⁻¹/mass fraction, with no meaningful distinction between the behavior of R₁ and R₂ or meaningful historical variation. (The values quoted here are representative of the historical variability and are not the result of statistical calculation.) Within the experimental scatter, the separability of composition and temperature effects holds (i.e., β_C and β_T are independent).

4. Discussion

Perhaps the most striking feature of the fluorescence energy coefficients cited above is the historical consistency of the values, particularly those coefficients relating fluorescence energy changes to variations in pressure (Table 1) and temperature (Table 3). Extending over a 40 year period, most pressure coefficient measurements fell within a 1 % relative variation, and over a 60 year period, most temperature coefficient

measurements fell within a 0.5 % relative variation. There are probably several (unsurprising and interrelated) reasons for this consistency: First, both pressure and temperature are scalars, and thus formulations relating fluorescence energy shifts to pressure and temperature, both experimentally and theoretically, are relatively simple. Second, pressure and temperature are fundamental thermodynamic parameters, and thus the experimental infrastructure is well established (e.g., instrumented DACs) for measuring their effects. Third, the historical consistency probably reflects an example of “convergent publication,” in which values are reported *only* if they are consistent with previously published values. Notwithstanding the potential absence of some results and the often absence of uncertainties, the coefficients determining pressure and temperature effects (in the linear range) on fluorescence energies in alumina are accurate and precise.

The simplest meanings of the pressure and temperature coefficients are embodied in their units. A 1 cm⁻¹ of energy shift in the R-lines will be caused by 132 MPa (0.132 GPa = 1 cm⁻¹/[7.6 cm⁻¹/GPa]) of equitriaxial stress (hydrostatic pressure when negative or compressive); see Eq. (5) and Table 1. This is a very small pressure for a DAC, and the energy shift is modest (with adequate sampling, this shift is easily detected, e.g., Ref. [67, 135]; for an R₁ shift of 14 403 cm⁻¹ to 14 402 cm⁻¹, this corresponds to a wavelength increase from 694.30 nm to 694.35 nm). A 1 cm⁻¹ energy shift will also be caused by about 7 K of temperature excursion (7.1 K = 1 cm⁻¹/[0.140 cm⁻¹/K]; again, easily applied and measured); see Eq. (13) and Table 3. To place these effects in atomic-scale context, it should be realized that 132 MPa of equitriaxial stress corresponds to a volume strain of 5.2×10^{-4} (using a linear bulk modulus of 253 GPa [2]). That is, to first approximation, the volume of the O²⁻ octahedron surrounding the substitutional Cr³⁺ ion undergoes a relative volume change of 5.2×10^{-4} , and the O²⁻-Cr³⁺ separation undergoes a relative length change of about 0.08: The spectroscopic effects of stress are large because the changes to the crystal field (as quantified by the ionic separation) are large. A similar approximation leading to a similar conclusion can be made using the volume thermal expansion coefficient (about 17×10^{-6} K⁻¹ [163]), resulting in a relative ionic separation change of about 0.05 for a temperature change of 7 K.

Historical and between-laboratory consistency is slightly weak in the case of coefficients relating fluorescence energy changes to changes in the tensor stress field (Table 2) and to changes in composition (Table 4): Most stress tensor component measurements fell within a 4 % relative variation, and the composition coefficient measurements exhibited a 25 % relative variation. In both cases, there is a limited sample set, so it is difficult to draw definitive conclusions regarding accuracy and precision. Ma and Clarke [44] argued that the value of the coefficient relating energy shift to composition in Table 4 is about right (it is accurate). They cited an explicit measurement of density variation with composition to arrive at a dilatational strain that was used in a mechanics analysis for positive comparison with pressure experiments (in a similar use of relative volume to compare experiments as in the shock work [150, 151]). A 1 cm⁻¹ energy shift will be caused by changes in composition of about 0.008 mass fraction of Cr in Al₂O₃:Cr (0.008 = 1 cm⁻¹/[120 cm⁻¹/mass fraction]; see Eq. (14) and Table 4. This composition, about 0.002 substitution of Cr³⁺ for Al³⁺, is too small, even given the ionic radius increase (see Introduction), to generate the octahedral dilatations inferred for pressure and temperature effects and yet begins to approach that of “heavily doped” ruby, in which Cr³⁺-Cr³⁺ pair-wise interaction effects cannot be ignored [160]. Clearly, more research is required on the composition coefficient. (The gross variations in emission color and intensity with Cr composition were noted in the very earliest—1850s—observations of Al₂O₃:Cr luminescence [164].)

A constraint is placed on the components of the piezospectroscopic tensor Π_{ij} , in that the trace of this tensor must yield the piezospectroscopic pressure coefficient from Eqs. (4) and (5). However, in only two cases (Table 2) have the sums $\Pi_a^{(x)} + \Pi_m^{(x)} + \Pi_c^{(x)}$ [45] or $2\Pi_a^{(x)} + \Pi_c^{(x)}$ [146] been checked to show agreement with the known values of $\Pi_p^{(x)}$, and in both cases, uncertainties in the components were not given, so the significance is difficult to judge. In both cases in which $\Pi_m^{(x)}$ was measured separately from $\Pi_a^{(x)}$ [45, 148], subsequent digitization and fitting to estimate uncertainties (in the work here) led to different estimates for the *mean* coefficients, further confusing the significance of the results. Nevertheless, the *mean* and *constrained value* estimates (Table 2) for both the individual coefficients and their sums have accuracies comparable to their precisions. (Some works have mis-cited other works, leading to more

confusion. For example: Langer [143] and Forman [16] incorrectly cited Paetzold [142] as $\Pi_a^{(1)} = 9.5$ and $\Pi_a^{(2)} = 8.4$ and $\Pi_a^{(1)} = 9.3$ and $\Pi_a^{(2)} = 8.2$, respectively; Grabner [38], Molis [42], and He [45] incorrectly cited Schawlow [140] for $\Pi_a^{(x)}$, $\Pi_c^{(x)}$, and $\Pi_p^{(x)}$ values, when no values were provided; Grabner [38] incorrectly cited Kaplyanskii [146] as $\Pi_a^{(1)} = 3.2$, $\Pi_p^{(1)} = 7.8$, $\Pi_a^{(2)} = 2.8$, and $\Pi_p^{(2)} = 7.5$; Ma [58] incorrectly cited Kaplyanskii [158] for Π values, when no values were provided; He [45] incorrectly cited Kaplyanskii [146] as $\Pi_a^{(1)} = 3.2$ and $\Pi_a^{(2)} = 2.8$; and Ma [43] and He [45] incorrectly cited Feher [148] as $\Pi_a^{(1)} = 2.7$, $\Pi_c^{(1)} = 1.8$, $\Pi_a^{(2)} = 2.4$, and $\Pi_c^{(2)} = 2.2$. Other works cited values “to be published” that never appeared, e.g., Ref. [59]. The above works should not be cited in support of coefficient values.)

Some tests of apparently uniaxial geometry were in fact tests of single-crystal- or polycrystal-orientation averaging rather than tests of individual tensor coefficients. It should be noted that the undifferentiated sum $2\Pi_a^{(x)} + \Pi_c^{(x)}$ appears as the single-crystal *pressure* coefficient in Eq. (5), averaging over all single-crystal loading orientations, and as the *polycrystal* coefficient in Eq. (12), averaging over all arbitrarily loaded polycrystal grain orientations. The shock tests [150, 151] make explicit comparison with the single-crystal pressure tests. Fiber measurements were compared with the predicted polycrystalline average values, e.g., Refs. [82, 88], as were the uniaxial or bending polycrystal measurements [42, 43, 90]. These tests were good measures of the sum (which is well known; Table 1), but could not distinguish individual piezospectroscopic components. Similar limited conclusions can be made regarding biaxial tests and comparison with the polycrystalline prediction [100].

A major goal of this review is to assess the state of fluorescence piezospectroscopic coefficients for use in measuring and mapping stress distributions in bulk polycrystalline alumina. In addition to considering the historical context of the coefficients and the likely accuracy and precision as above, it is worth considering the relative sizes of the effects of stress, temperature, and composition in a typical fluorescence measurement. Incorporating temperature and composition coefficients explicitly into Eq. (1a) gives

$$\Delta\nu_\sigma = \Delta\nu - \beta_T(T - T_{\text{ref}}) - \beta_C C. \quad (1a')$$

Assuming that a reference experiment is conducted on a (typically sapphire) specimen of known stress state (zero), temperature (adjusted to a reference point, often 298.8 K), and composition (near zero Cr), the net fluorescence shift $\Delta\nu$ for the target alumina is easily determined (as ν_0 is now well known). Typical large values are $\Delta\nu^{(1)} = -0.80 \text{ cm}^{-1}$ and $\Delta\nu^{(2)} = -0.60 \text{ cm}^{-1}$ [67]. A typical value for T is $21 \text{ }^\circ\text{C} = 294.15 \text{ K}$. A typical value for C for alumina is 0.0001. Equation (1a') thus becomes (using Tables 3 and 4)

$$\Delta\nu_\sigma^{(1)} = -0.80 - (-0.14)(-4.65) - (120)(0.0001) = -0.80 - 0.65 - 0.01 = -1.46 \text{ cm}^{-1},$$

$$\Delta\nu_\sigma^{(2)} = -0.60 - (-0.14)(-4.65) - (120)(0.0001) = -0.60 - 0.65 - 0.01 = -1.26 \text{ cm}^{-1}.$$

Two features are apparent in the above calculations: Temperature effects (the second terms in the third equalities) are large comparable to the overall stress effect, and composition effects (the third terms) are small, probably negligible. Even a range of net shifts (as is observed in Ref. [67], $\pm 0.8 \text{ cm}^{-1}$, reflecting a range of stress states and peak shifts) does not alter these conclusions.

Continuing on to typical calculations for a polycrystal: Using the *constrained values* in Table 2 and Eq. (10) yields $\Pi_M^{(1)} = \Pi_M^{(2)} = 7.60 \text{ cm}^{-1}/\text{GPa}$, $\Pi_S^{(1)} = -1.34 \text{ cm}^{-1}/\text{GPa}$, and $\Pi_S^{(2)} = -0.32 \text{ cm}^{-1}/\text{GPa}$. In combination with typical values of $\Delta\nu_\sigma^{(1)} = -1.46 \text{ cm}^{-1}$ and $\Delta\nu_\sigma^{(2)} = -1.26 \text{ cm}^{-1}$ measured at a single point in a polycrystal as above, Eq. (11) leads to $\sigma_M = -158 \text{ MPa}$ and $\sigma_S = 196 \text{ MPa}$. If $\Delta\nu = -1.46 \text{ cm}^{-1}$ represents the shift averaged over many points in a random polycrystal under uniaxial stress, then Eq. (12) leads to $\sigma_u = -1.46/(7.6/3) = -577 \text{ MPa}$.

For a thermally grown oxide random polycrystal film under biaxial stress, the stress levels of many gigapascals lead to fluorescence energy shifts of many wavenumbers [96–119], and the temperature and composition “corrections” above are unnecessary. Similarly, unless there is a comparison of results from different measurement methods, e.g., between shock and static pressure [150], or with a model, e.g., Ref.

[58], temperature and composition corrections are not necessary. In these cases, relative measurements are adequate, as shown by the large number of application works cited in the Introduction (about 70) compared with the smaller number of calibration works cited in the Results (about 30). The large stresses observed in many thermally grown oxide films suggest that nonlinear effects might be important in these systems (similar to those observed in Fig. 5). Using a refined crystal field model calibrated to the known nonlinear observations [45, 115, 150, 151], Margueron and Clarke [58] suggested a quadratic fit for the polycrystalline R₂ line shift under hydrostatic pressure of about $\Delta\nu_p^{(2)} = -7.62p - 0.0046p^2$, where the pressure p has units of GPa. For a pressure of 2 GPa, the quadratic contribution to the shift is about 0.02 cm⁻¹. As a *correction* to an estimate of stress, this value is negligible relative to the shifts considered above. When treated as an *uncertainty*, however, this value is about twice the uncertainty associated with line position. However, as shown below, both are small (but not negligible) relative to temperature effects. Raman spectroscopy, electron backscatter diffraction, and X-ray diffraction [138] could all be used on thermally grown oxide films to independently calibrate nonlinear effects.

For a bulk polycrystal, not only are the corrections necessary, but the uncertainties in the quantities on the right side of Eq. (1a) must be considered. Assuming that the positions of either peak of the R₁ and R₂ fluorescence lines can be determined with an experimental uncertainty of $u(\Delta\nu^{(x)}) = 0.01 \text{ cm}^{-1}$ [67], and using the information in Tables 3 and 4, the uncertainty in the stress-related shift, $u(\Delta\nu_\sigma)$, is given by summing the absolute uncertainties in quadrature [165], taking $u(\beta_T) = 0.007 \text{ cm}^{-1}/\text{K}$ and $u(\beta_T) = 30 \text{ cm}^{-1}/\text{mass fraction}$,

$$\begin{aligned} u(\Delta\nu_\sigma) &= [u^2(\Delta\nu) + (u(\beta_T) * 4.65)^2 + (u(\beta_C) * 0.0001)^2]^{1/2} \\ &\approx [10^{-4} + 10^{-3} + 10^{-5}]^{1/2} = 0.035 \text{ cm}^{-1}. \end{aligned}$$

The second line of this equation has been written to make clear that the greatest contribution to the uncertainty in the stress shift is the uncertainty in the temperature coefficient (the middle term). Temperature corrections are a necessity for accurate and precise stress determinations by fluorescence shifts. Nevertheless, the relative uncertainty in the stress shift is only $(0.035/1.46) \approx 2.3\%$, and Table 2 and Eq. (11) show that this term dominates the uncertainty in the stress calculation. Hence, the uncertainty in $\sigma_M = -158 \text{ MPa}$ calculated above is $u(\sigma_M) \approx 4 \text{ MPa}$ (given exactly by summing all the *relative* uncertainties in quadrature [165]). The stress uncertainty is small, making clear why the fluorescence method is effective for estimating stress and stress distributions [43, 59, 66, 67] in bulk polycrystalline alumina.

Acknowledgments

The authors thank Drs. Y. B. Gerbig and D. L. Kaiser, both of National Institute of Standards and Technology (NIST), and Dr. S. Margueron of Université de Lorraine et Centrale Supélec, for careful review of the manuscript.

5. References

- [1] Burns R (2005) *Mineralogical Applications of Crystal Field Theory* (Cambridge University Press, Cambridge), 2nd Ed.
- [2] Syassen K (2008) Ruby under pressure. *High Pressure Research* 28(2):75–126. <https://doi.org/10.1080/08957950802235640>.
- [3] Moss S, Newnham R (1964) The chromium position in ruby. *Zeitschrift für Kristallographie* 120(4–5):359–363. <https://doi.org/10.1524/zkri.1964.120.4-5.359>.
- [4] Brown G Jr (1964) Fluorescence lifetimes of ruby. *Journal of Applied Physics* 35:3062–3063. <https://doi.org/10.1063/1.1713175>.
- [5] Tanabe Y, Sugano S (1954) On the absorption spectra of complex ions. I. *Journal of the Physical Society of Japan* 9(5):753–766. <https://doi.org/10.1143/JPSJ.9.753>.
- [6] Tanabe Y, Sugano S (1954) On the absorption spectra of complex ion. II. *Journal of the Physical Society of Japan* 9(5):766–779. <https://doi.org/10.1143/JPSJ.9.766>.
- [7] Tanabe Y, Sugano S (1956) On the absorption spectra of complex ions, III. The calculation of the crystal field strength. *Journal of the Physical Society of Japan* 11(8):864–877. <https://doi.org/10.1143/JPSJ.11.864>.

- [8] Tanabe Y, Kamimura H (1958) On the absorption spectra of complex ions, IV. The effect of the spin-orbit interaction and the field of lower symmetry on d electrons in cubic field. *Journal of the Physical Society of Japan* 13(4):394–411. <https://doi.org/10.1143/JPSJ.13.394>.
- [9] Sugano S, Tanabe, Y (1958) Absorption spectra of Cr^{3+} Al_2O_3 . Part A. Theoretical studies of the absorption bands and lines. *Journal of the Physical Society of Japan* 13(8):880–899. <https://doi.org/10.1143/JPSJ.13.880>.
- [10] Sugano S, Tsujikawa I (1958) Absorption spectra of Cr^{3+} Al_2O_3 . Part B. Experimental studies of the Zeeman effect and other properties of the line spectra. *Journal of the Physical Society of Japan* 13(8):899–910. <https://doi.org/10.1143/JPSJ.13.899>.
- [11] McClure D (1962) Optical spectra of transition-metal ions in corundum. *Journal of Chemical Physics* 36(10):2757–2779. <https://doi.org/10.1063/1.1732364>.
- [12] Macfarlane R (1963) Analysis of the spectrum of d^3 ions in trigonal crystal fields. *Journal of Chemical Physics* 39(11):3118–3126. <https://doi.org/10.1063/1.1734152>.
- [13] Poole C Jr (1964) The optical spectra and color of chromium containing solids. *Journal of Physics and Chemistry of Solids* 25(11):1169–1182. [https://doi.org/10.1016/0022-3697\(64\)90014-9](https://doi.org/10.1016/0022-3697(64)90014-9).
- [14] Devlin G, McKenna J, May A, Schawlow A (1962) Composite rod optical masers. *Applied Optics* 1(1):11–15. <https://doi.org/10.1364/AO.1.000011>.
- [15] Collins R, Nelson D, Schawlow A, Bond W, Garrett C, Kaiser W (1960) Coherence, narrowing, directionality, and relaxation oscillations in the light emissions from ruby. *Physical Review Letters* 5(7):303–305. <https://doi.org/10.1103/PhysRevLett.5.303>.
- [16] Forman R, Piermarini G, Barnett J, Block S (1972) Pressure measurement made by the utilization of ruby sharp-line luminescence. *Science* 176(4032):284–285. <https://doi.org/10.1126/science.176.4032.284>.
- [17] Barnett J, Block S, Piermarini G (1973) An optical fluorescence system for quantitative pressure measurement in the diamond-anvil cell. *Review of Scientific Instruments* 44(1):1–9. <https://doi.org/10.1063/1.1685943>.
- [18] Hawke R, Syassen K, Holzapfel W (1974) An apparatus for high pressure Raman spectroscopy. *Review of Scientific Instruments* 45(12):1598–1601. <https://doi.org/10.1063/1.1686569>.
- [19] Piermarini G, Block S (1975) Ultrahigh pressure diamond-anvil cell and several semiconductor phase transition pressures in relation to the fixed point pressure scale. *Review of Scientific Instruments* 46(8):973–979. <https://doi.org/10.1063/1.1134381>.
- [20] Piermarini G, Block S, Barnett J, Forman R (1975) Calibration of the pressure dependence of the R_1 ruby fluorescence line to 195 kbar. *Journal of Applied Physics* 46(6):2774–2780. <https://doi.org/10.1063/1.321957>.
- [21] Adams D, Appleby R, Sharma S (1976) Spectroscopy at very high pressures: Part X. Use of ruby R-lines in the estimation of pressure at ambient and at low temperatures. *Journal of Physics E: Scientific Instruments* 9:1140–1144. <https://doi.org/10.1088/0022-3735/9/12/034>.
- [22] Mao H, Bell P, Shaner J, Steinberg D (1978) Specific volume measurements of Cu, Mo, Pd, and Ag and calibration of the ruby R_1 fluorescence pressure gauge from 0.06 to 1 Mbar. *Journal of Applied Physics* 49(6):3276–3283. <https://doi.org/10.1063/1.325277>.
- [23] Wunder S, Schoen P (1981) Pressure measurement at high temperatures in the diamond anvil cell. *Journal of Applied Physics* 52(6):3772–3775. <https://doi.org/10.1063/1.329841>.
- [24] Xu J, Mao H, Bell P (1986) High-pressure ruby and diamond fluorescence: observations at 0.21 to 0.55 Terapascal. *Science* 232(4756):1404–1406. <https://doi.org/10.1126/science.232.4756.1404>.
- [25] Mao H, Xu J, Bell P (1986) Calibration of the ruby pressure gauge to 800 kbar under quasi-hydrostatic conditions. *Journal of Geophysical Research* 91(B5):4673–4676. <https://doi.org/10.1029/JB091iB05p04673>.
- [26] Eggert J, Goettel K, Silvera I (1989) Ruby at high pressure. I. Optical line shifts to 156 GPa. *Physical Review B* 40(8):5724–5732. <https://doi.org/10.1103/PhysRevB.40.5724>.
- [27] Eggert J, Goettel K, Silvera I (1989) Ruby at high pressure. II. Fluorescence lifetime of the R line to 130 GPa. *Physical Review B* 40(8):5733–5738. <https://doi.org/10.1103/PhysRevB.40.5733>.
- [28] Vos W, Schouten J (1991) On the temperature correction to the ruby pressure scale. *Journal of Applied Physics* 69(9):6744–6746. <https://doi.org/10.1063/1.348903>.
- [29] Fujishiro I, Nakamura Y, Yamanokuchi H (1994) Evaluation of temperature dependence on ruby fluorescence at high pressure by viscosity measurement of lubricants. *AIP Conference Proceedings* 309:1059–1062. <https://doi.org/10.1063/1.46286>.
- [30] Chai M, Brown J (1996) Effects of static non-hydrostatic stress on the R lines of ruby single crystals. *Geophysical Research Letters* 23(24):3539–3542. <https://doi.org/10.1029/96GL03372>.
- [31] Chen N, Silvera I (1996) Excitation of ruby fluorescence at multimegabar pressures. *Review of Scientific Instruments* 67(12):4275–4278. <https://doi.org/10.1063/1.1147526>.
- [32] Rekhi R, Dubrovinsky L, Saxena S (1999) Temperature-induced ruby fluorescence shifts up to a pressure of 15 GPa in an externally heated diamond anvil cell. *High Temperatures-High Pressures* 31(3):299–305. <https://doi.org/10.1068/htrt161>.
- [33] Holzapfel W (2003) Refinement of the ruby luminescence pressure scale. *Journal of Applied Physics* 93(3):1813–1818. <https://doi.org/10.1063/1.1525856>.
- [34] Chijioka A, Nellis W, Soldatov A, Silvera I (2005) The ruby pressure standard to 150 GPa. *Journal of Applied Physics* 98:114905. <https://doi.org/10.1063/1.2135877>.
- [35] Silvera I, Chijioka A, Nellis W, Soldatov A, Temper J (2007) Calibration of the ruby pressure scale to 150 GPa. *Physica Status Solidi (b)* 244(1):460–467. <https://doi.org/10.1002/pssb.200672587>.
- [36] Goncharov A, Zaug J, Crowhurst J, Gregoryanz E (2005) Optical calibration of pressure sensors for high pressures and temperatures. *Journal of Applied Physics* 97(094917). <https://doi.org/10.1063/1.1895467>.
- [37] Yamaoka H, Zekko Y, Jarrige I, Lin J, Hiraoka N, Ishii H, Tsuei K, Mizuki J (2012) Ruby pressure scale in a low-temperature diamond anvil cell. *Journal of Applied Physics* 112:124503. <https://doi.org/10.1063/1.4769305>.
- [38] Grabner L (1978) Spectroscopic technique for the measurement of residual stress in sintered Al_2O_3 . *Journal of Applied Physics* 49(2):580–583. <https://doi.org/10.1063/1.324682>.
- [39] Blendell J, Coble R, Charles R (1976) On the relaxation of stresses arising from thermal expansion anisotropy during cooling polycrystalline materials. *Ceramic Microstructures*, ed. Fulrath RM, Pask JA (Westview Press, Boulder) pp 721–730.

- [40] Blendell J, Coble R (1982) Measurement of stress due to thermal expansion anisotropy in Al_2O_3 . *Journal of the American Ceramic Society* 65(3):174–178. <https://doi.org/10.1111/j.1151-2916.1982.tb10390.x>.
- [41] Song H, French R, Coble R (1989) Effect of residual strain on the electronic structure of alumina and magnesia. *Journal of the American Ceramic Society* 72(6):990–994. <https://doi.org/10.1111/j.1151-2916.1989.tb06257.x>.
- [42] Molis S, Clarke D (1990) Measurement of stresses using fluorescence in an optical microprobe: Stresses around indentations in a chromium-doped sapphire. *Journal of the American Ceramic Society* 73(11):3189–3194. <https://doi.org/10.1111/j.1151-2916.1990.tb06435.x>.
- [43] Ma Q, Clarke D (1993) Stress measurement in single-crystal and polycrystalline ceramics using their optical fluorescence. *Journal of the American Ceramic Society* 76(6):1433–1440. <https://doi.org/10.1111/j.1151-2916.1993.tb03922.x>.
- [44] Ma Q, Clarke D (1993) Optical fluorescence from chromium ions in sapphire: A probe of the image stress. *Acta Metallurgica et Materialia* 41(6):1811–1816. [https://doi.org/10.1016/0956-7151\(93\)90201-3](https://doi.org/10.1016/0956-7151(93)90201-3).
- [45] He J, Clarke D (1995) Determination of the piezospectroscopic coefficients for chromium-doped sapphire. *Journal of the American Ceramic Society* 78(5):1347–1353. <https://doi.org/10.1111/j.1151-2916.1995.tb08493.x>.
- [46] Lipkin D, Clarke D (1995) Sample-probe interactions in spectroscopy: Sampling microscopic property gradients. *Journal of Applied Physics* 77(5):1855–1863. <https://doi.org/10.1063/1.358885>.
- [47] Kizler P, He J, Clarke D, Kenway P (1996) Structural relaxation around substitutional Cr^{3+} ions in sapphire. *Journal of the American Ceramic Society* 79(1):3–11. <https://doi.org/10.1111/j.1151-2916.1996.tb07873.x>.
- [48] He J, Clarke D (1997) Polarization dependence of the Cr^{3+} R-line fluorescence from sapphire and its application to crystal orientation and piezospectroscopic measurement. *Journal of the American Ceramic Society* 79(1):3–11. <https://doi.org/10.1111/j.1151-2916.1997.tb02792.x>.
- [49] Atkinson A, Jain S, Webb S (1999) Convolution of spectra in optical microprobe experiments. *Semiconductor Science and Technology* 14:561–564. <https://doi.org/10.1088/0268-1242/14/6/312>.
- [50] Yu H, Clarke D (2002) Effect of codoping on the R-line luminescence of Cr^{3+} -doped alumina. *Journal of the American Ceramic Society* 85(8):1966–1970. <https://doi.org/10.1111/j.1151-2916.2002.tb00389.x>.
- [51] Wan K, Zhu W, Pezzotti G (2006) Methods of piezo-spectroscopic calibration of thin-film materials: I. Ball-on-ring biaxial flexure. *Measurement Science and Technology* 17(1):181–190. <https://doi.org/10.1088/0957-0233/17/1/029>.
- [52] Zhu W, Wan K, Pezzotti G (2006) Methods of piezo-spectroscopic calibration of thin-film materials: II. Tensile stress field at indentation crack tip. *Measurement Science and Technology* 17(1):191–198. <https://doi.org/10.1088/0957-0233/17/1/030>.
- [53] Margueron S, Clarke D (2007) Stress anisotropy of the R-line luminescence lifetime in single crystal Cr-doped sapphire (ruby). *Journal of Applied Physics* (101):093521. <https://doi.org/10.1063/1.2727443>.
- [54] Margueron S, eClarke D (2007) Effect of polarization and uniaxial stress on the R-line luminescence of single crystal sapphire. *Journal of Applied Physics* (101):093902. <https://doi.org/10.1063/1.2717155>.
- [55] Margueron S, Clarke D (2007) Effect of residual stress on the luminescence lifetime of R-line emission from polycrystalline alumina formed by oxidation. *Journal of the American Ceramic Society* 90(6):1798–1801. <https://doi.org/10.1111/j.1151-2916.2007.01635.x>.
- [56] Guo S, Todd R (2010) Confocal fluorescence microscopy in alumina-based ceramics: Where does the signal come from? *Journal of the European Ceramic Society* 30(3):641–648. <https://doi.org/10.1016/j.jeurceramsoc.2009.08.020>.
- [57] Gao R, Li H, Zhao J (2015) Dependence of R fluorescence lines of rubies on Cr^{3+} concentration at various temperatures, with implications for pressure calibrations in experimental apparatus. *American Mineralogist* 100:1554–1561. <https://doi.org/10.1111/j.1151-2916.2002.tb00389.x>.
- [58] Margueron S, Clarke D (2015) Refined crystal field model for the piezospectroscopy analysis of stresses in polycrystalline alumina. *Journal of Applied Physics* (118):094503. <https://doi.org/10.1063/1.4929960>.
- [59] Ma Q, Clarke D (1994) Piezospectroscopic determination of residual stresses in polycrystalline alumina. *Journal of the American Ceramic Society* 77(2):298–302. <https://doi.org/10.1111/j.1151-2916.1994.tb06996.x>.
- [60] Dauskardt R, Ager J III (1996) Quantitative stress mapping in alumina composites by optical fluorescence imaging. *Acta Materialia* 44(2):625–641. [https://doi.org/10.1016/1359-6454\(95\)00189-1](https://doi.org/10.1016/1359-6454(95)00189-1).
- [61] Toyoda T, Obikawa T, Shigenari T (1998) Photoluminescence spectroscopy of Cr^{3+} in ceramic Al_2O_3 . *Materials Science and Engineering B* 54(1–2): 33–37. [https://doi.org/10.1016/S0921-5107\(98\)00122-6](https://doi.org/10.1016/S0921-5107(98)00122-6).
- [62] Jankowiak R, Roberts K, Tomasiak P, Sikora M, Small G, Schilling C (2000) Probing the crystalline environment of α -alumina via luminescence of metal ion impurities: An optical method of ceramic flaw detection. *Materials Science and Engineering A* 281(1–2): 45–55. [https://doi.org/10.1016/S0921-5093\(99\)00749-2](https://doi.org/10.1016/S0921-5093(99)00749-2).
- [63] Narita Y, Murotani H (2002) Submicrometer optical characterization of the grain boundary of optically active Cr^{3+} doped polycrystalline Al_2O_3 by near-field spectroscopy. *American Mineralogist* 87:1144–1147. <https://doi.org/10.2138/am-2002-8-912>.
- [64] Kortov V, Ermakov A, Zatsepin A, Nikiforov S (2008) Luminescence properties of nanostructured alumina ceramic. *Radiation Measurements* 43:341–344. <https://doi.org/10.1016/j.radmeas.2007.10.008>.
- [65] Liu Q, Yang Q, Zhao G, Lu S, Zhang H (2013) The thermoluminescence and optically stimulated luminescence properties of Cr-doped alpha alumina transparent ceramics. *Journal of Alloys and Compounds* 579:259–262. <https://doi.org/10.1016/j.jallcom.2013.06.070>.
- [66] Myers G, Michaels C, Cook R (2016) Quantitative mapping of stress heterogeneity in polycrystalline alumina using hyperspectral fluorescence microscopy. *Acta Materialia* 106:272–282. <https://doi.org/10.1016/j.actamat.2016.01.020>.
- [67] Michaels C, Cook R (2016) Determination of residual stress distributions in polycrystalline alumina using fluorescence microscopy. *Materials & Design* 107:478–490. <https://doi.org/10.1016/j.matdes.2016.06.063>.
- [68] Ma Q, Pompe W, French J, Clarke D (1994) Residual stresses on $\text{Al}_2\text{O}_3\text{-ZrO}_2$ composites: A test of stochastic stress models. *Acta Metallurgica et Materialia* 42(5):1673–1681. [https://doi.org/10.1016/0956-7151\(94\)90377-8](https://doi.org/10.1016/0956-7151(94)90377-8).
- [69] Sergo V, Clarke D, Pompe W (1995) Deformation bands in ceria-stabilized zirconia/alumina: I, measurement of internal stresses. *Journal of the American Ceramic Society* 78(3):633–640. <https://doi.org/10.1111/j.1151-2916.1995.tb08224.x>.

- [70] Sergo V, Clarke D (1995) Deformation bands in ceria-stabilized zirconia/alumina: II, stress-induced aging at room temperature. *Journal of the American Ceramic Society* 78(3):641–644. <https://doi.org/10.1111/j.1151-2916.1995.tb08225.x>.
- [71] Sergo V, Lipkin D, De Portu G, Clarke D (1997) Edge stresses in alumina/zirconia laminates. *Journal of the American Ceramic Society* 80(7):1633–1638. <https://doi.org/10.1111/j.1151-2916.1997.tb03031.x>.
- [72] Sergo V, Pezzotti G, Sbaizer O, Nishida T (1998) Grain size influence on residual stresses on alumina/zirconia composites. *Acta Materialia* 46(5):1701–1710. [https://doi.org/10.1016/S1359-6454\(97\)00348-0](https://doi.org/10.1016/S1359-6454(97)00348-0).
- [73] Pardo J, Merino R, Orera V, Peña J, González C, Pastor J, LLorca J (2000) Piezospectroscopic study of residual stresses in Al_2O_3 - ZrO_2 directionally solidified eutectics. *Journal of the American Ceramic Society* 83(11):2745–2752. <https://doi.org/10.1111/j.1151-2916.2000.tb01626.x>.
- [74] Ortiz Merino J Todd R (2003) Thermal microstress measurements in Al_2O_3 /SiC nanocomposites by Cr^{3+} fluorescence microscopy. *Journal of the European Ceramic Society* 23(11):1779–1783. [https://doi.org/10.1016/S0955-2219\(02\)00446-6](https://doi.org/10.1016/S0955-2219(02)00446-6).
- [75] Peña J, Larsson M, Merino R, de Francisco I, Orera V, LLorca J, Pastor J, Martín, Segurado J (2006) Processing, microstructure and mechanical properties of directionally-solidified Al_2O_3 - $\text{Y}_3\text{Al}_5\text{O}_{12}$ - ZrO_2 ternary eutectics. *Journal of the European Ceramic Society* 26(15):3113–3121. <https://doi.org/10.1016/j.jeurceramsoc.2005.11.005>.
- [76] Perrière L, Valle R, Carrère N, Gouadec G, Colombe Ph, Lartigue-Korinek S, Mazerolles L, Parlier M (2011) Crack propagation and stress distribution in binary and ternary directionally solidified eutectic ceramics. *Journal of the European Ceramic Society* 31(7):1199–1210. <https://doi.org/10.1016/j.jeurceramsoc.2010.09.016>.
- [77] Gouadec G, Makoui K, Perrière L, Colombe Ph, Mazerolles L (2012) Ruby micro-piezospectroscopy in $\text{GdAlO}_3/\text{Al}_2\text{O}_3/\text{ZrO}_2$, $\text{Er}_3\text{Al}_5\text{O}_{12}/\text{Al}_2\text{O}_3/\text{ZrO}_2$ and $\text{Y}_3\text{Al}_5\text{O}_{12}/\text{Al}_2\text{O}_3/\text{ZrO}_2$ binary and ternary directionally solidified eutectics. *Journal of the European Ceramic Society* 32(10):2145–2151. <https://doi.org/10.1016/j.jeurceramsoc.2012.01.038>.
- [78] Benamara O, Cherif M, Duffar T, Lebbou K (2015) Microstructure and crystallography of Al_2O_3 - $\text{Y}_3\text{Al}_5\text{O}_{12}$ - ZrO_2 ternary eutectic oxide grown by the micropulling down technique. *Journal of Crystal Growth* 429:27–34. <https://doi.org/10.1016/j.jcrysGro.2015.07.020>.
- [79] Liu H, Lim K, Jia W, Strauss E, Yen W, Buoncristiani A, Byvik C (1988) Effects of tensile stress on the R lines of Cr^{3+} in sapphire fiber. *Optics Letters* 13(10):931–933. <https://doi.org/10.1364/OL.13.000931>.
- [80] Ma Q, Clarke D (1993) Measurement of residual stresses in sapphire fiber composites using optical fluorescence. *Acta Metallurgica et Materialia* 41(6):1817–1823. [https://doi.org/10.1016/0956-7151\(93\)90202-4](https://doi.org/10.1016/0956-7151(93)90202-4).
- [81] Ma Q, Liang L, Clarke D, Hutchinson J (1994) Mechanics of the push-out process from *in situ* measurement of the stress distribution along embedded sapphire fibers. *Acta Metallurgica et Materialia* 42(10):3299–3308. [https://doi.org/10.1016/0956-7151\(94\)90462-6](https://doi.org/10.1016/0956-7151(94)90462-6).
- [82] Yang X, Young R (1995) Determination of residual strains in ceramic-fibre reinforced composites using fluorescence spectroscopy. *Acta Metallurgica et Materialia* 43(6):2407–2416. [https://doi.org/10.1016/0956-7151\(94\)00438-2](https://doi.org/10.1016/0956-7151(94)00438-2).
- [83] Young R, Yang X (1996) Interfacial failure in ceramic fibre/glass composites. *Composites Part A* 27:737–741. [https://doi.org/10.1016/1359-835X\(96\)00022-X](https://doi.org/10.1016/1359-835X(96)00022-X).
- [84] Yallee R, Andrews M, Young R (1996) Fragmentation in alumina fibre reinforced epoxy model composites monitored using fluorescence spectroscopy. *Journal of Materials Science* 31(13):3349–3359. <https://doi.org/10.1007/BF00360734>.
- [85] He J, Clarke D (1997) Determination of fibre strength distributions from bundle tests using optical luminescence spectroscopy. *Proceedings of the Royal Society of London A* 453(1954):1881–1901. <https://doi.org/10.1098/rspa.1997.0101>.
- [86] Belnap J, Shetty D (1998) Micromechanics of crack bridging in sapphire/epoxy composites. *Composites Science and Technology* 58(11):1763–1773. [https://doi.org/10.1016/S0266-3538\(98\)00042-6](https://doi.org/10.1016/S0266-3538(98)00042-6).
- [87] Mahiou H, Beakou A, Young R (1999) Investigation into stress transfer characteristics in alumina-fibre/epoxy model composites through the use of fluorescence spectroscopy. *Journal of Materials Science* 34(24):6069–6080. <https://doi.org/10.1023/A:1004705500981>.
- [88] He J, Beyerlein I, Clarke D (1999) Load transfer from broken fibers in continuous fiber Al_2O_3 -Al composites and dependence on local volume fraction. *Journal of the Mechanics and Physics of Solids* 47(3):465–502. [https://doi.org/10.1016/S0022-5096\(98\)00053-2](https://doi.org/10.1016/S0022-5096(98)00053-2).
- [89] Sinclair R, Young R, Martin R (2004) Determination of the axial and radial fibre stress distributions for the Broutman test. *Composites Science and Technology* 64(2):181–189. [https://doi.org/10.1016/S0266-3538\(03\)00257-4](https://doi.org/10.1016/S0266-3538(03)00257-4).
- [90] Dassios K, Galiotis C (2004) Fluorescence studies of polycrystalline Al_2O_3 composite constituents: piezo-spectroscopic calibration and applications. *Appl. Phys. A* 79(3):647–659. <https://doi.org/10.1007/s00339-002-2075-3>.
- [91] Belnap J, Shetty D (2005) Interfacial properties of sapphire/epoxy composites: Comparison of fluorescence spectroscopy and fiber push-in techniques. *Composites Science and Technology* 65(11–12):1851–1860. <https://doi.org/10.1016/j.compscitech.2005.03.013>.
- [92] Wen Q, Clarke D, Yu N, Nastasi M (1995) Epitaxial regrowth of ruby on sapphire for an integrated thin film stress sensor. *Applied Physics Letters* 66(3):293–295. <https://doi.org/10.1063/1.113522>.
- [93] Wen Q, Ma, Q, Clarke D (1994) *In-situ* fluorescence strain sensing of the stress in interconnects. *Thin Films and Mechanical Properties V, MRS Proceedings* 356:591–598. <https://doi.org/10.1557/PROC-356-591>.
- [94] Yu N, Wen Q, Clarke D, McIntyre P, Kung H, Nastasi M, Simpson T, Mitchell I, Li D (1995) Formation of iron or chromium doped epitaxial sapphire thin films on sapphire substrates. *Journal of Applied Physics* 78(9):5412–5421. <https://doi.org/10.1063/1.359722>.
- [95] Kumari S, Khare A (2011) Note: Epitaxial ruby thin film based photonic sensor for temperature measurement. *Review of Scientific Instruments* 82:066106. <https://doi.org/10.1063/1.3606443>.
- [96] Lipkin D, Clarke D (1996) Measurement of the stress in oxide scales formed by oxidation of alumina-forming alloys. *Oxidation Metals* 45(3/4):267–280. <https://doi.org/10.1007/BF01046985>.
- [97] Christensen R, Lipkin D, Clarke D, Murphy K (1996) Nondestructive evaluation of the oxidation stresses through thermal barrier coatings using Cr^{3+} piezospectroscopy. *Journal of Applied Physics* 69(24):3752–3756. <https://doi.org/10.1063/1.117182>.

- [98] Christensen R, Lipkin D, Clarke D (1996) The stress and spalling behavior of the oxide scale formed on polycrystalline Ni₃Al. *Acta Materialia* 44(9):3813–3821. [https://doi.org/10.1016/1359-6454\(96\)00009-2](https://doi.org/10.1016/1359-6454(96)00009-2).
- [99] Gong X, Clarke D (1998) On the measurement of strain in coatings formed on a wrinkled elastic substrate. *Oxidation Metals* 50(6/5):355–376. <https://doi.org/10.1023/A:1018848607100>.
- [100] Tolpygo V, Clarke D (1998) Competition between stress generation and relaxation during oxidation of an Fe-Cr-Al-Y alloy. *Oxidation Metals* 49(1/2):187–212. <https://doi.org/10.1023/A:1018828619028>.
- [101] Tolpygo V, Clarke D (1998) Wrinkling of α -alumina films grown by thermal oxidation—I. Quantitative studies on single crystals of Fe-Cr-Al alloy. *Acta Materialia* 46(14):5153–5166. [https://doi.org/10.1016/S1359-6454\(98\)00133-5](https://doi.org/10.1016/S1359-6454(98)00133-5).
- [102] Tolpygo V, Clarke D (1998) Wrinkling of α -alumina films grown by thermal oxidation—II. Oxide separation and failure. *Acta Materialia* 46(14):5167–5174. [https://doi.org/10.1016/S1359-6454\(98\)00134-7](https://doi.org/10.1016/S1359-6454(98)00134-7).
- [103] Tolpygo V, Clarke D (2000) Spalling failure of α -alumina films grown by oxidation: I. Dependence on cooling rate and metal thickness. *Materials Science and Engineering A* 278:142–150. [https://doi.org/10.1016/S0921-5093\(99\)00581-X](https://doi.org/10.1016/S0921-5093(99)00581-X).
- [104] Tolpygo V, Clarke D (2000) Spalling failure of α -alumina films grown by oxidation: II. Decohesion nucleation and growth. *Materials Science and Engineering A* 278:151–161. [https://doi.org/10.1016/S0921-5093\(99\)00582-1](https://doi.org/10.1016/S0921-5093(99)00582-1).
- [105] Schlichting K, Vaidyanathan K, Sohn Y, Jordan E, Gell M, Padture N (2000) Application of Cr³⁺ photoluminescence piezospectroscopy to plasma-sprayed thermal barrier coatings for residual stress measurement. *Materials Science and Engineering A* 291:68–77. [https://doi.org/10.1016/S0921-5093\(00\)00973-4](https://doi.org/10.1016/S0921-5093(00)00973-4).
- [106] Atkinson A, Selçuk A, Webb S (2000) Variability of stress in alumina corrosion layers formed in thermal-barrier coatings. *Oxidation Metals* 54(5/6):371–384. <https://doi.org/10.1023/A:100461332338>.
- [107] Nychka J, Clarke D (2001) Damage quantification in TBCs by photo-stimulated luminescence spectroscopy. *Surface and Coatings Technology* 146–147:110–116. [https://doi.org/10.1016/S0257-8972\(01\)01455-4](https://doi.org/10.1016/S0257-8972(01)01455-4).
- [108] Selçuk A, Atkinson A (2002) Analysis of the Cr³⁺ luminescence spectra from thermally grown oxide in thermal barrier coatings. *Materials Science and Engineering A* 335:147–156. [https://doi.org/10.1016/S0921-5093\(01\)01911-6](https://doi.org/10.1016/S0921-5093(01)01911-6).
- [109] Selçuk A, Atkinson A (2003) The evolution of residual stress in the thermally grown oxide on Pt diffusion bond coats in TBCs. *Acta Materialia* 51(2):535–549. [https://doi.org/10.1016/S1359-6454\(02\)00436-6](https://doi.org/10.1016/S1359-6454(02)00436-6).
- [110] Nychka J, Clarke D, Sridharan S, Jordan E, Gell M, Lance M, Chunnilall C, Smith I, Saunders S, Pillane R, Sergio V, Selçuk A, Atkinson A, Murphy K (2003) NDE assessment of TBCs: An interim report of a photo-stimulated luminescence ‘round-robin’ test. *Surface and Coatings Technology* 163–164:87–94. [https://doi.org/10.1016/S0257-8972\(02\)00596-0](https://doi.org/10.1016/S0257-8972(02)00596-0).
- [111] Nychka J, Xu T, Clarke D, Evans A (2004) The stresses and distortions caused by formation of a thermally grown alumina: Comparison between measurements and simulations. *Acta Materialia* 52(9):2561–2568. <https://doi.org/10.1016/j.actamat.2004.02.004>.
- [112] Peng X, Sridhar N, Clarke D (2004) The stress distribution around holes in thermal barrier coatings. *Materials Science and Engineering A* 380:208–214. <https://doi.org/10.1016/j.msea.2004.03.062>.
- [113] Tomimatsu T, Zhu S, Kagawa Y (2004) Local stress distribution in thermally-grown-oxide layer by near-field optical microscopy. *Scripta Materialia* 50(1):137–141. <https://doi.org/10.1016/j.scriptamat.2003.09.005>.
- [114] Hovis A, Heuer A (2005) Confocal photo-stimulated microspectroscopy (CPSM)—Residual stress measurements in Al₂O₃ using confocal microscopy. *Scripta Materialia* 53(3):347–349. <https://doi.org/10.1016/j.scriptamat.2005.04.016>.
- [115] Margueron S, Clarke D (2006) The use of polarization in the piezospectroscopic determination of the residual stresses in polycrystalline alumina films. *Acta Materialia* 54(20):5551–5557. <https://doi.org/10.1016/j.actamat.2006.08.017>.
- [116] Ohtsuka S, Zhu W, Tochino S, Sekiguchi Y, Pezzotti G (2007) In-depth analysis of residual stress in an alumina coating on silicon nitride substrate using confocal Raman piezo-spectroscopy. *Acta Materialia* 55(4):1129–1135. <https://doi.org/10.1016/j.actamat.2006.05.038>.
- [117] Clarke D, Gardiner D (2007) Recent advances in piezospectroscopy. *International Journal of Materials Research* 98(8):756–762. <https://doi.org/10.3139/146.101528>.
- [118] Gardiner D, Bowden M, Margueron S, Clarke D (2007) Use of polarization in imaging the residual stresses in polycrystalline alumina films. *Acta Materialia* 55(10):3431–3436. <https://doi.org/10.1016/j.actamat.2007.01.044>.
- [119] Heeg B, Tolpygo V, Clarke D (2011) Damage evolution in thermal barrier coatings with thermal cycling. *Journal of the American Ceramic Society* 94(S1):S112–S119. <https://doi.org/10.1111/j.1551-2916.2011.04496.x>.
- [120] Ostertag C, Robins L, Cook L (1991) Cathodoluminescence measurement of strained alumina single crystals. *Journal of the European Ceramic Society* 7(2):109–116. [https://doi.org/10.1016/0955-2219\(91\)90008-N](https://doi.org/10.1016/0955-2219(91)90008-N).
- [121] Pezzotti G, Sbaizer O, Sergio V, Muraki N, Maruyama K, Nishida T (1998) *In situ* measurements of frictional bridging stresses in alumina using fluorescence spectroscopy. *Journal of the American Ceramic Society* 81(1):187–192. <https://doi.org/10.1111/j.1551-2916.1998.tb02312.x>.
- [122] Pezzotti G (1999) *In situ* study of fracture mechanisms in advanced ceramics using fluorescence and Raman microprobe spectroscopy. *Journal of Raman Spectroscopy* 30(10):867–875. [https://doi.org/10.1002/\(SICI\)1097-4555\(199910\)30:10<867::AID-JRS466>3.0.CO;2-0](https://doi.org/10.1002/(SICI)1097-4555(199910)30:10<867::AID-JRS466>3.0.CO;2-0).
- [123] Pezzotti G, Okuda H, Muraki N, Nishida T (1999) *In-situ* determination of bridging stresses in Al₂O₃/Al₂O₃-platelet composites by fluorescence spectroscopy. *Journal of the European Ceramic Society* 19(5):601–608. [https://doi.org/10.1016/S0955-2219\(98\)00230-1](https://doi.org/10.1016/S0955-2219(98)00230-1).
- [124] Pezzotti G, Suenobu H, Nishida T (1999) Measurement of microscopic bridging stresses in an alumina/molybdenum composite by *in situ* fluorescence spectroscopy. *Journal of the American Ceramic Society* 82(5):1257–1262. <https://doi.org/10.1111/j.1551-2916.1999.tb01904.x>.
- [125] Banini G, Chaudhri M, Smith T, Hayward I (2001) Measurement of residual stresses around Vickers indentations in a ruby crystal using a Raman luminescence microscope. *Journal of Physics D: Applied Physics* 34:L122–L124. <https://doi.org/10.1088/0022-3727/34/22/103>.

- [126] Pezzotti G, Müller W (2002) Micromechanics of fracture in a ceramic/metal composite studied by *in situ* fluorescence spectroscopy I: Foundations and stress analysis. *Continuum Mechanics and Thermodynamics* 14(1):113–126. <https://doi.org/10.1007/s001610100076>.
- [127] Todd R, Stowe D, Galloway S, Barnes D, Wilshaw P (2008) Piezospectroscopic measurement of the stress field around an indentation crack tip in ruby using SEM cathodoluminescence. *Journal of the European Ceramic Society* 28(10):2049–2055. <https://doi.org/10.1016/j.jeurceramsoc.2008.02.008>.
- [128] Wu H, Roberts S, Derby B (2008) Residual stress distributions around indentations and scratches in polycrystalline Al₂O₃ and Al₂O₃/SiC nanocomposites measured using fluorescence probes. *Acta Materialia* 56(1):140–149. <https://doi.org/10.1016/j.actamat.2007.09.014>.
- [129] Guo S, Todd R (2010) Cr³⁺ microspectroscopy measurements and modelling of local variations in surface grinding stresses in polycrystalline alumina. *Journal of the European Ceramic Society* 30(12):2533–2545. <https://doi.org/10.1016/j.jeurceramsoc.2010.04.016>.
- [130] Guo S, Limpichaipanit A, Todd R (2011) High resolution optical microprobe investigation of surface grinding stresses in Al₂O₃ and Al₂O₃/SiC nanocomposites. *Journal of the European Ceramic Society* 31(1–2):97–109. <https://doi.org/10.1016/j.jeurceramsoc.2010.08.021>.
- [131] Guo S, Todd R (2011) Quantitative optical fluorescence microprobe measurements of stresses around indentations in Al₂O₃ and Al₂O₃/SiC nanocomposites: The influence of depth resolution and specimen translucency. *Acta Materialia* 59(7):2637–2647. <https://doi.org/10.1016/j.actamat.2010.12.055>.
- [132] Dancer C, Curtis H, Bennett S, Petrinic N, Todd R (2011) High strain rate indentation-induced deformation in alumina ceramics measured by Cr³⁺ fluorescence mapping. *Journal of the European Ceramic Society* 31(13):2177–2187. <https://doi.org/10.1016/j.jeurceramsoc.2011.06.002>.
- [133] Greene R, Gallops S, Fünfschilling S, Fett T, Hoffmann M, Ager J III, Kružić J (2012) A direct comparison of non-destructive techniques for determining bridging stress distributions. *Journal of the Mechanics and Physics of Solids* 60(8):1462–1477. <https://doi.org/10.1016/j.jmps.2012.04.007>.
- [134] Huang S, Binnera J, Vaidhyanathan B, Todd R (2014) Quantitative analysis of the residual stress and dislocation density distributions around indentations in alumina and zirconia toughened alumina (ZTA) ceramics. *Journal of the European Ceramic Society* 34(3):753–763. <https://doi.org/10.1016/j.jeurceramsoc.2013.09.021>.
- [135] Munro R, Piermarini G, Block S, Holzapfel W (1985) Model line-shape analysis for the ruby R lines used for pressure measurement. *Journal of Applied Physics* 57(2):165–169. <https://doi.org/10.1063/1.334837>.
- [136] Grasset O (2001) Calibration of the R ruby fluorescence lines in the pressure range [0–10 GP] and the temperature range [250–300 K]. *High Pressure Research* 21:139–157. <https://doi.org/10.1080/08957950108201020>.
- [137] Mase G (1970) *Continuum Mechanics* (The McGraw-Hill Companies, New York).
- [138] Friedman L, Vaudin M, Stranick S, Stan G, Gerbig Y, Osborn W, Cook R (2016) Assessing strain mapping by electron backscatter diffraction and confocal Raman microscopy using wedge-indented Si. *Ultramicroscopy* 163:75–86. <https://doi.org/10.1016/j.ultramic.2016.02.001>.
- [139] Kaplyanskii A, Przhevuskii A, Roezenbaum R (1969) Concentration-dependent line-shift in optical spectra of ruby. *Soviet Physics—Solid State* 10(8):1864–1868.
- [140] Schawlow A (1961) Fine structure and properties of chromium fluorescence in aluminum and magnesium oxide. *Advances in Quantum Electronics*, ed Singer JR (Columbia University Press, New York), pp 50–64.
- [141] Gibson U, Chernuschenko M (1999) Ruby films as surface temperature and pressure sensors. *Optics Express* 4(11):443–448. <https://doi.org/10.1364/OE.4.000443>.
- [142] Paetzold H (1951) Über den Temperatur- und Druckeinfluss auf Elektronenterme in Kristallen. *Zeitschrift für Physik* 129(2):123–139 (in German). <https://doi.org/10.1007/BF01333392>.
- [143] Langer D, Euwema R (1967) Pressure shift of the Cr levels in Al₂O₃. *Journal of the Physics and Chemistry of Solids* 28(3):463–465. [https://doi.org/10.1016/0022-3697\(67\)90315-0](https://doi.org/10.1016/0022-3697(67)90315-0).
- [144] Ragan D, Clarke D, Schiferl D (1996) Silicone fluid as a high-pressure medium in diamond anvil cells. *Review of Scientific Instruments* 67(2):494–496. <https://doi.org/10.1063/1.1146627>.
- [145] Liu L, Bi Y, Xu J (2013) Ruby fluorescence pressure scale: Revisited. *Chinese Physics B* 22(5):056201-1–5. <https://doi.org/10.1088/1674-1056/22/5/056201>.
- [146] Kaplyanskii A, Przhevuskii A (1962) The piezospectroscopic effect in ruby crystals. *Soviet Physics—Doklady* 7(1):37–40.
- [147] Sturge M (1965) Effect of stress on the level splittings of ruby: Origin of the ground-state splitting. *Journal of Chemical Physics* 43(5):1826–1827. <https://doi.org/10.1063/1.1697015>.
- [148] Feher E, Sturge M (1968) Effect of stress on the trigonal splittings of d^3 ions in sapphire (α -Al₂O₃). *Physical Review* 172(2):244–249. <https://doi.org/10.1103/PhysRev.172.244>.
- [149] Fujishiro I, Nakamura Y, Kawase T, Okai B (1988) The property of a ruby high pressure sensor under uniaxial compressive stress. *Japan Society of Mechanical Engineers International Journal Series* 3 31(1):136–141. <https://doi.org/10.1299/jsmec1988.31.136>.
- [150] Horn P, Gupta Y (1989) Luminescence R-line spectrum of ruby crystals shocked to 125 kbar along the crystal c axis. *Physical Review B* 39(2):973–979. <https://doi.org/10.1103/PhysRevB.39.973>.
- [151] Gupta Y, Shen X (1991) Potential use of the ruby R₂ line shift for static high-pressure calibration. *Applied Physics Letters* 58 (6):583–585. <https://doi.org/10.1063/1.104594>.
- [152] McCumber D, Sturge M (1963) Linewidth and temperature shift of the R lines in ruby. *Journal of Applied Physics* 34(6):1682–1684. <https://doi.org/10.1063/1.1702657>.
- [153] Powell R, DiBartolo B, Birang B, Naiman C (1966) Temperature dependence of the widths and positions of the R and N lines in heavily doped ruby. *Journal of Applied Physics* 37(13):4973–4978. <https://doi.org/10.1063/1.1708175>.
- [154] Yen J, Nicol M (1992) Temperature dependence of the ruby luminescence method for measuring high pressures. *Journal of Applied Physics* 72(12):5535–5538. <https://doi.org/10.1063/1.351950>.

- [155] Ragan D, Gustavsen R, Schiferl D (1992) Calibration of the ruby R₁ and R₂ fluorescence shifts as a function of temperature from 0 to 600 K. *Journal of Applied Physics* 72(12):5539–5544. <https://doi.org/10.1063/1.351951>.
- [156] Huang T-H, Hsu C-C, Kuo C-T, Lu P, Tse, W-S, Wang D, Chou T, Fuh A (1994) Ruby spectral band-profile analysis for temperature sensing. *Journal of Applied Physics* 75(7):3599–3606. <https://doi.org/10.1063/1.356071>.
- [157] Powell R, DiBartolo B, Birang, B, Naiman C (1967) Fluorescence studies of energy transfer between single and pair Cr³⁺ systems in Al₂O₃. *Physical Review* 155(2):296–308. <https://doi.org/10.1103/PhysRev.155.296>.
- [158] Kaplyanskii A, Przhevskii A (1967) Deformational splitting of luminescence spectrum lines and the structure of exchange-linked pairs of chromium ions in ruby. *Soviet Physics—Solid State* 9(1):190–198.
- [159] Mollenauer L, Schwallow A (1968) Piezospectroscopic studies of exchange-coupled Cr³⁺ ion pairs in ruby. *Physical Review* 168(2):309–317. <https://doi.org/10.1103/PhysRev.168.309>.
- [160] Powell R, DiBartolo B (1972) Review Article: Optical properties of heavily doped ruby. *Physica Status Solidi (a)* 10(2):315–357. <https://doi.org/10.1002/pssa.2210100202>.
- [161] Williams Q, Jeanloz R (1985) Pressure shift of Cr³⁺-ion-pair emission lines in ruby. *Physical Review B* 31(11):7449–7451. <https://doi.org/10.1103/PhysRevB.31.7449>.
- [162] Margueron S (2017) Private communication of unpublished work.
- [163] Anderson A (1995) *Equations of State of Solids for Geophysics and Ceramic Science* (Oxford University Press, Oxford).
- [164] Becquerel E (1859) Recherches sur divers effets lumineux qui résultent de l'action de la lumière sur les corps. *Annales de Chimie et de Physique* 17(3):40–128. <http://gallica.bnf.fr/ark:/12148/bpt6k65671381/f511.item>.
- [165] Taylor J (1997) *An Introduction to Error Analysis* (University Science Books, Herndon, VA), 2nd Ed.

About the authors: Dr. Robert F. Cook is a NIST Fellow in the Materials Measurement Science Division at NIST. Dr. Cook performs research on mechanics and mechanical behavior of materials, with a focus on fracture and deformation of brittle materials.

Dr. Chris A. Michaels is a Research Chemist in the Materials Measurement Science Division at NIST. Dr. Michaels develops and applies high-spatial-resolution spectroscopic techniques and instrumentation to the study of materials.

The National Institute of Standards and Technology is an agency of the U.S. Department of Commerce.